

## **Title**

Deglacial reconstruction of the spatial extent and intensity of the North Atlantic Subtropical High

## **Authors**

David Fastovich\*<sup>1</sup> (ORCID: 0000-0002-0340-9819)  
Tripti Bhattacharya<sup>2</sup> (ORCID: 0000-0002-5528-3760)  
Stephen T. Jackson<sup>3</sup> (ORCID: 0000-0002-1487-4652)  
Teresa R. Krause<sup>4</sup> (ORCID: 0000-0003-0211-5189)  
James M. Russell<sup>5</sup> (ORCID: ?)  
Timothy M. Shanahan<sup>6</sup> (ORCID: 0000-0002-3831-3198)  
Chijun Sun<sup>7</sup> (ORCID: 0000-0002-3668-346X)  
John W. Williams<sup>8</sup> (ORCID: 0000-0001-6046-9634)

\*Corresponding author, fastovich@uga.edu

<sup>1</sup>Department of Geography, University of Georgia, Athens, GA, USA

<sup>2</sup>Department of Earth and Environmental Sciences, Syracuse University, Syracuse, NY, USA

<sup>3</sup>National and Regional Climate Adaptation Science Centers, U.S. Geological Survey, Tucson, AZ, USA, and Department of Geosciences, University of Arizona, Tucson, AZ, USA

<sup>4</sup>Department of Biology, Augsburg University, Minneapolis, MN, USA

<sup>5</sup>Department of Earth, Environmental & Planetary Sciences, Brown University, Providence, RI, USA

<sup>6</sup>Department of Earth and Planetary Sciences, Jackson School of Geosciences, The University of Texas at Austin, Texas, USA

<sup>7</sup>Department of Earth and Planetary Sciences, University of California, Davis, Davis, CA USA

<sup>8</sup>Department of Geography and Center for Climatic Research, University of Wisconsin-Madison, Madison, WI, USA

## **Peer-review Statement**

This manuscript has been submitted to Nature Geoscience and is not peer-reviewed. This preprint has been submitted to EarthArXiv. Subsequent versions of this manuscript may have slightly different content. If accepted, the final version of this manuscript will be available via the 'Peer-reviewed Publication DOI' link on the right-hand side of this webpage.

## **CRedit (Contributor Roles Taxonomy)**

David Fastovich - Conceptualization, Formal analyses, Funding acquisition, Investigation, Methodology, Project administration, Software, Validation, Visualization, Writing - original draft  
Tripti Bhattacharya - Conceptualization, Funding acquisition, Investigation, Methodology, Resources, Supervision, Writing – review & editing  
Stephen T. Jackson - Writing – review & editing, Investigation  
Teresa R. Krause - Writing – review & editing, Investigation  
James M. Russell - Writing – review & editing, Investigation  
Timothy M. Shanahan - Writing – review & editing, Investigation  
Chijun Sun - Writing – review & editing, Investigation  
John W. Williams - Writing – review & editing, Investigation

### **Keywords**

Hydroclimate, Leaf wax, precipitation isotopes, paleoclimate, deglaciation, atmospheric circulation

## Main Text

### 1. Introduction

Southeastern North America (SENA) faces intensifying rainfall over the coming century (1, 2), posing risks to life, property, and economic activity. Although the largest changes are expected over coming decades, their early consequences are already evident. The cumulative cost of rainfall damages from flooding was between \$39 and \$91 billion from 1988 to 2017 across the United States (3), with the greatest rainfall increases expected in SENA (1). Accurate climate projections are necessary to address these accelerating challenges but coupled land-atmosphere-ocean models pose challenges for simulating precipitation in SENA. For instance, northward moisture transport along the western edge of the North Atlantic Subtropical High (NASH) is the largest moisture source in SENA (4, 5), and is itself coupled to regional and North Atlantic sea surface temperature (6, 7) and the configuration of the Northern Hemisphere Hadley Cell (8, 9). Substantial internal variability (e.g., North Atlantic Oscillation and Atlantic Multidecadal Variability) within each coupled component makes it difficult to isolate and identify the specific processes governing SENA hydroclimate. Constraining hydroclimate responses to different forcing mechanisms is needed to disentangle these controls and improve hydroclimate projections, which in turn requires longer-term perspectives that the instrumental record cannot provide.

The most recent deglaciation is well-suited to constrain SENA hydroclimate response to forced changes in greenhouse gases, ice sheet configuration, and ocean circulation. Following the Last Glacial Maximum, atmospheric carbon dioxide increased by  $\sim 80$  ppm (10) which caused ice sheet loss (11, 12) and subsequent ocean heat transport variability (13). These forcings evolved asynchronously, and included both gradual and abrupt transitions, enabling isolation of their individual effects on SENA hydroclimate. However, a lack of unambiguous hydroclimate proxies has meant that few constraints exist for deglacial hydroclimate evolution in SENA. Fossil-pollen reconstructions have been among the few empirical approaches to understanding deglacial rainfall changes in SENA (14–16), but both traditional (17) and machine-learning approaches (18) are limited by precipitation's secondary role in determining temperate forest composition (19).

Leaf wax biomarkers can constrain the patterns and drivers of SENA hydroclimate. These long-chain *n*-alkanes are readily preserved in sediments across SENA and are significantly correlated to the hydrogen isotopic signature of precipitation ( $\delta D_p$ ) (20). This proxy fidelity allows the application of leaf-wax stable isotope hydroclimate reconstructions to identify changes in atmospheric circulation, moisture sources, and precipitation amount across diverse environments (21–24). We examine hydroclimate dynamics across the last deglaciation in SENA using the hydrogen-isotope composition of leaf-wax biomarkers from White Pond, South

Carolina (34.168 °N, 80.777 °W) and Hall's Cave, Texas (30.136 °N, -99.535 °W) (25). Together, these two records are used to reconstruct the spatial extent and intensity of the NASH across the last deglaciation. The processes controlling deglacial evolution of the NASH are constrained with a suite of isotope-enabled climate models that provide insights into future rainfall extremes.

## **2. Results and Discussion**

### **2.1 Contemporary Climatology of the North Atlantic Subtropical High and $\delta D_p$ as a Tracer**

Contemporary climatology indicates a close link between hydrogen isotopes in precipitation ( $\delta D_p$ ) and upstream variability in the NASH (Figure 1). Moisture from the Gulf of Mexico is the largest source of water vapor into SENA (5) (Figure 1A). Zonal pressure gradients between SENA and the NASH are responsible for northward flow that delivers this moisture into SENA (Figure S1). Therefore, these northward winds and corresponding moisture advection into SENA are directly tied to the NASH.

Water vapor enriched in deuterium over the Gulf of Mexico (Figure S2) makes this moisture transport traceable in the water isotopes of precipitation ( $\delta D_p$ ). As this water vapor is advected into SENA, the deuterium-enriched vapor produces rainfall with a distinct deuterium-enriched fingerprint across SENA (Figure 1A). Meanwhile, low meridional moisture transport in the Great Lakes, New England, and Canada indicates deuterium-depleted  $\delta D_p$  (Figure 1A).

The relationship between  $\delta D_p$  and meridional moisture transport in SENA (Figure 2B) suggests that northward transport of moisture from the Gulf of Mexico by the NASH is a primary control on SENA  $\delta D_p$ , overwhelming processes like distillation from continentality. For example, along a meridional transect at 88.5°W between 30–37.5°N,  $\delta D_p$  decreases 7‰ across 830 km of inland transport (Figure 1B). This decrease is far less than observed in other midlatitude regions such as the western United States, where  $\delta D_p$  decreases by 40‰ to 80‰ over 80 to 500 km (26, 27) and in Europe, where  $\delta D_p$  decreases by 16‰ over 1,000 km (28) (here, we convert reported  $\delta^{18}O_p$  values to  $\delta D_p$ , assuming equilibrium Rayleigh distillation).

### **2.2 A Regional Approach and Index for Reconstructing the North Atlantic Subtropical High Intensity and Extent**

Northward moisture flux into SENA has an asymmetric response to variability in the spatial extent and intensity of the NASH. To quantify this variability directly from reanalysis data, we define the Bermuda High Index (BHI) as the difference in standardized mean sea level pressure between the western edge of the NASH (25.38 - 29.38 °N, 85 - 80 °W) and Great Plains (35 - 39

°N, 105.5 - 100 °W) (dashed boxes in Figure 1C, D, S1 Supplemental Information) (29). BHI provides an instrumental target that we aim to reconstruct.

Compositing BHI values reveals two distinct hydroclimate responses across SENA to variability in the intensity and spatial extent of the NASH (Figure 1C, D). Under a westward-expanded ( $BHI \geq 90$ th percentile) or eastern-contracted ( $BHI \leq 10$ th percentile) NASH, meridional moisture transport anomalies are small along the Atlantic Coastal Plain (Figure 1C, 1D). In other words, the Atlantic Coastal Plain sits within the typical spatial footprint of the NASH. Therefore, we posit that northward moisture flux into the Atlantic Coastal Plain records the *intensity* of meridional moisture transport along the western edge of the NASH. An increase in meridional moisture transport along the Atlantic Coastal Plain would increase  $\delta D_p$  from enhanced transport of deuterium-enriched vapor from the Gulf of Mexico (Figure S2). Meanwhile, prior analyses of  $\delta D_p$  in the southern Great Plains attribute decreases in  $\delta D_p$  to increases in stratiform rainfall from mesoscale convective systems fueled by moisture transport from the Great Plains Low Level Jet (30). The Great Plains Low Level Jet is coupled to the NASH through a geostrophic response to the zonal pressure gradient across the Great Plains (25, 31–33). In this way, a westward expansion in the NASH leads to a large increase in northward moisture transport in the southern Great Plains (Figure 1C, 1D) and corresponding increase in the likelihood of mesoscale convective activity and decrease in  $\delta D_p$  (30). Therefore, unlike the positive relationship between the NASH, meridional moisture transport, and  $\delta D_p$  along the Atlantic Coastal Plain, a negative relationship is expected in the southern Great Plains. This suggests that unlike the Atlantic Coastal Plain,  $\delta D_p$  in the southern Great Plains is sensitive to the *spatial extent* of the NASH.

Asymmetric moisture flux responses in SENA to variability in the spatial extent and intensity of the NASH indicate that observations from both the Atlantic Coastal Plain and the southern Great Plains are needed to completely characterize the NASH, as either region alone conflates NASH intensity and spatial extent. We resolve this by taking the difference in  $\delta D_{wax}$  from a site in the Atlantic Coastal Plain (White Pond) and southern Great Plains (Hall's Cave) (25) after standardizing both records (Figure 1C, 1D, 2A, 2B), to define a leaf-wax-based reconstruction of NASH variability,  $\Delta \delta D_{NASH_{leaf\ wax}}$ . The resulting zonal  $\delta D_{wax}$  gradient reconstructs the intensity (White Pond) and spatial extent (Hall's Cave) of the NASH in a way that a single-site reconstruction cannot (Figure 1C, 1D). We reproduce  $\Delta \delta D_{NASH_{leaf\ wax}}$  using ERA5 meteorological variables in place of  $\delta D_{wax}$ : meridional vapor transport and average rainfall rate. Both correlate significantly with mean sea level pressure over the Gulf of Mexico (reflecting NASH spatial extent) and over the western Atlantic (reflecting NASH intensity), supporting our use of zonal  $\delta D_{wax}$  gradients in SENA to reconstruct the spatial extent and intensity of the NASH (Figure S3).

### 2.3 Asymmetric North Atlantic Subtropical High response across the last deglaciation

At White Pond,  $\delta D_{\text{wax}}$  remains high until  $\sim 15$  to  $14$  ka, indicating elevated transport of deuterium-enriched  $\delta D_{\text{vapor}}$  moisture from the Gulf of Mexico into the southeastern United States, driven by a stronger NASH. A subsequent gradual decrease in  $\delta D_{\text{wax}}$  at White Pond closely tracks summer insolation and ice sheet loss, suggesting a gradual decrease in northward moisture from a weakening of the NASH in response to increasing temperatures (Figure 2A). In contrast,  $\delta D_{\text{wax}}$  at Hall's Cave, TX demonstrates high millennial-scale variability (Figure 2B). Deglacial millennial-scale variability in the NASH wind speed has previously been shown to be inversely related to north Atlantic sea surface temperatures (34). The similarity between Hall's Cave  $\delta D_{\text{wax}}$  and north Atlantic sea surface temperatures (Figure 2B) supports this interpretation that a westward expansion of the NASH from decreased temperatures would increase stratiform rainfall and decrease  $\delta D_{\text{wax}}$ .

Combining White Pond and Hall's Cave  $\delta D_{\text{wax}}$  into a reconstruction of the intensity and spatial extent of NASH ( $\Delta \delta D \text{ NASH}_{\text{leaf wax}}$ , Figure 3C) identifies two distinct modes of behavior. The first mode is a weakening and contraction of the NASH in response to deglacial warming between  $15.4$  and  $10.5$  ka (Figure 2C). The second mode is an abrupt intensification and expansion in response to a weakening of the Atlantic Meridional Overturning Circulation (AMOC) that operates at millennial timescales and is particularly evident between  $13.7$  ka and  $12$  ka (Figure 2C).

Gradual weakening and contraction of the NASH in the first mode is indicated by the decrease in  $\Delta \delta D \text{ NASH}_{\text{leaf wax}}$  from  $\sim 1$  at  $15.4$  ka to  $\sim -2$  at  $10.5$  ka. Positive  $\Delta \delta D \text{ NASH}_{\text{leaf wax}}$  between  $18$  ka and  $15$  ka reflect above-average  $\delta D_{\text{wax}}$  at White Pond, driven by a stronger NASH that increases the flux of deuterium-enriched Gulf of Mexico water vapor into the site (Figure 2, S4A). During this same interval Hall's Cave  $\delta D_{\text{wax}}$  is below average from increased stratiform rainfall, fueled by elevated Gulf of Mexico moisture transport, thereby increasing the zonal  $\delta D_{\text{wax}}$  gradient across SENA (Figure 2, S4G). Collectively, these site-level changes, summarized in  $\Delta \delta D \text{ NASH}_{\text{leaf wax}}$ , suggest that the late-glacial ( $18$  ka to  $15$  ka) NASH was stronger and larger relative to the Holocene ( $11$  ka to  $10$  ka). The NASH weakened after  $\sim 15$  ka as White Pond  $\delta D_{\text{wax}}$  decreased below mean values and contracted eastward as Hall's Cave  $\delta D_{\text{wax}}$  increased above mean values (Figure S4). Large Northern Hemisphere ice loss at  $\sim 15$  ka, may explain the long-term NASH weakening and contraction inferred from  $\Delta \delta D \text{ NASH}_{\text{leaf wax}}$  (Figure 2A, 2B, 2C). In Last Glacial Maximum climate model experiments, high albedo produces an intensification of the NASH, hence an albedo decrease from ice loss would weaken the NASH (35, 36).

An abrupt increase in the  $\Delta \delta D \text{ NASH}_{\text{leaf wax}}$  to  $\sim 1$  near the Younger Dryas suggests a westward expansion of the NASH caused by cooling of north Atlantic sea surface temperatures from a reduction in the AMOC (Figure 2B, 2C, 2D). A westward expansion decreases  $\delta D_{\text{wax}}$  at Hall's Cave below mean values from increased stratiform rainfall fueled by concentrated moisture

transport toward Hall's Cave from an expanded NASH, increasing  $\Delta\delta D \text{ NASH}_{\text{leaf wax}}$  (Figure 2C, S4G). Notably, White Pond  $\delta D_{\text{wax}}$  shows no abrupt deviation across the Younger Dryas, suggesting NASH intensity did not change appreciably during this interval, only its spatial extent (Figure 2C, S4A).

The North Atlantic Oscillation has long served as analogue for interpreting patterns of Atlantic temperature and atmospheric circulation change during reductions of AMOC strength (34, 37, 38), in part because direct proxy evidence of changes in the NASH or the Icelandic Low has been lacking.  $\Delta\delta D \text{ NASH}_{\text{leaf wax}}$  directly probes the intensity and spatial extent of NASH and clarifies that the NASH may not only have intensified as previously inferred (34, 37, 38), but also expanded westward (Figure 2). Alternatively, the NASH may have expanded westward without intensification. However, Heinrich Event 1 likely had a larger reduction in the AMOC (13), yet  $\Delta\delta D \text{ NASH}_{\text{leaf wax}}$  suggests little change to the NASH (Figure 2C, 2D). We propose that the sensitivity of NASH extent to AMOC perturbations depends on background climate state. Under nearly full-glacial boundary conditions (as during Heinrich Event 1), the NASH response is muted, whereas under intermediate conditions (as during the Younger Dryas), the NASH response is pronounced. This may be because sea ice extent was already extensive before Heinrich event cooling initiated (39).

## 2.4 Simulations of the North Atlantic Subtropical High and Proxy-Model Comparisons

To assess our proxy-inferred NASH reconstruction ( $\Delta\delta D \text{ NASH}_{\text{leaf wax}}$ ) and its causal mechanisms, we examine a suite of isotope-enabled Community Earth System Model (iCESM) experiments. Within these experiments we reproduce  $\Delta\delta D \text{ NASH}_{\text{leaf wax}}$  with simulated  $\delta D_p$  by taking the standardized difference between simulated  $\delta D_p$  for the four grid cells surrounding White Pond and Hall's Cave, to define  $\Delta\delta D \text{ NASH}_{\text{iCESM}}$ . We distinguish the proxy reconstruction ( $\Delta\delta D \text{ NASH}_{\text{leaf wax}}$ ) from its model analogue ( $\Delta\delta D \text{ NASH}_{\text{iCESM}}$ ) using subscripts. For each iCESM experiment we take the difference between high ( $\geq 90$ th percentile) and low  $\Delta\delta D \text{ NASH}_{\text{iCESM}}$  years ( $\leq 10$ th percentile), which demonstrate that the zonal  $\delta D_p$  gradient across SENA appears closely coupled with the NASH (Figure 3).

In a simulation from 1979-2023 nudged to ERA5 reanalysis (WisOMIP) (40) and an un-nudged simulation of the last millennium (iLME, 850 to 2006) (41, 42), the zonal  $\delta D_p$  gradient increases as expected when the NASH expands westward, in agreement with our contemporary  $\delta D_p$  analyses and  $\delta D_{\text{wax}}$  proxy inferences (Figure 3A, 3B). However, in a transient, deglacial simulation (iTRACE) with greenhouse gas, ice sheet extent, ocean heat transport, and orbital forcings derived from proxy observations (43), the simulated zonal  $\delta D_p$  gradient across SENA increases when the NASH weakens and contracts eastward: an opposite relationship to our proxy records (Figure 3D). These findings indicate that iCESM1 accurately simulates the relationship between the zonal  $\delta D_p$  gradient in SENA and the NASH, but that the model struggles when

forcings beyond those of the last millennium or historical period are introduced. This modeling challenge is caused, in part, by the response of the Intertropical Convergence Zone to the AMOC which is erroneously linked to meridional moisture flux and corresponding  $\delta D_p$  at Hall's Cave in iTRACE (Supplementary Information).

Despite these modeling challenges, iTRACE partly simulates the response of the NASH to a weakening of the AMOC. Applying the same BHI defined from reanalysis (Section 2.2) to iTRACE's simulated pressure fields, enables comparing the simulated NASH to  $\Delta\delta D \text{ NASH}_{\text{leaf wax}}$ . The simulated NASH matches the millennial-scale variability in  $\Delta\delta D \text{ NASH}_{\text{leaf wax}}$  (Figure 4), which propagates to simulated integrated vapor transport and  $\delta D_p$ . High BHI values between 18 ka and 14 ka demonstrates that the NASH intensified and expanded westward, which increased simulated moisture flux at White Pond (Figure 4C, 4D). These coupled changes between simulated meridional vapor transport at White Pond and BHI appear linked to simulated sea surface temperatures in the North Atlantic (Figure 4E), and therefore the AMOC. Low North Atlantic sea surface temperatures force an intensification and expansion of the NASH, indicated by high BHI values, with downstream increases in meridional vapor transport at White Pond (Figure 4C, 4D, 4E). Critically, however, iTRACE fails to simulate a gradual weakening of the NASH, because BHI values for the Holocene (12 ka to 11 ka) are nearly identical to the late-glacial (20 ka to 19 ka) (Figure 4D).

This failure carries a troubling implication when extended to future extreme rainfall projections. Current projections indicate that the extreme rainfall is likely to become more common in SENA (1), with increases in SENA fall rainfall already linked to variability in the NASH (44). Yet, iTRACE reveals that models dramatically underestimate the NASH response to greenhouse gas increases, and therefore the moisture flux that supplies rainfall (Figure S4C, S4D, S4E). Since extreme rainfall scales with mean rainfall rates (45) and meridional moisture flux is a key ingredient for extreme rainfall in SENA (46), iTRACE is likely also underestimating past extreme rainfall. When placed alongside current extreme rainfall projections, our results support two conclusions. In the best case, ESMs may not produce confident projections of regional extreme rainfall. In the worst case, extreme rainfall in SENA may exceed latest ESM projections because these very models underestimate the NASH response in the past.

### 3. Conclusions

Our results demonstrate that the zonal  $\delta D_p$  and  $\delta D_{\text{wax}}$  gradient across SENA records changes in moisture delivered by the NASH to the region. Using this regional gradient, we show that the NASH weakened and contracted in response to gradual warming across the last deglaciation but intensified in response to a weakening in Atlantic Ocean heat transport. A transient, isotope-enabled climate model experiment (iTRACE) accurately simulates the responses of the NASH to a weakening of ocean heat transport, but underestimates responses to gradual deglacial

warming. Because Northern Hemisphere subtropical highs are expected to strengthen into the future (47), leading to increases in projected rainfall extremes in SENA (1), the inability of iTRACE to accurately simulate the response of the NASH to greenhouse-gas induced warming suggests that past and future simulations of extreme rainfall are poorly constrained and possibly underestimated. Future rainfall hazards may be less certain, and substantially larger, than currently projected.

## **Acknowledgements**

We gratefully acknowledge technical support from the Georgia Advanced Computing Resource Center and Stephanie Bullinger (Syracuse University). DF and TB acknowledge funding support from the National Science Foundation award AGS-2402498. TB acknowledges support from NSF CAREER Grant OCE-2237502 and Sloan Foundation Fellowship FG-2023-20259. White Pond was cored with support from NSF DEB-1353896. Initial lipid extraction at White Pond was supported by NSF DEB-1349662 and leaf wax biomarker measurements were made possible with support from NSF MRI Grant EAR-2018078.

## **Source Data**

All data, including derived iCESM fields (integrated vapor transport), along with analysis code and a containerized computing environment, are available on Zenodo (48). The original iCESM model output is not included due to its size but freely available from the National Science Foundation National Center for Atmospheric Research Geoscience Data Exchange (49, 50) and the NASA Center for Climate Simulation (40). White Pond, SC  $\delta D_{\text{wax}}$  measurements are also freely accessible on the NOAA Paleoclimatology Database and Zenodo (48). Hall's Cave, TX  $\delta D_{\text{wax}}$  is also accessible in the supplemental information of the original publication (25).

## **4. Materials and Methods**

### **4.1 Leaf wax analyses and $\delta D_{\text{wax}}$ measurements**

White Pond, SC was cored in April 2015 using a modified Livingstone square-rod piston corer, from which 5.85 meters of sediment were retrieved (51). Sediments were subsampled and processed using standard organic geochemical approaches to extract, purify, quantify, and measure leaf wax biomarkers in two stages. In 2015, sediments were first freeze-dried, homogenized, and all lipid compounds were extracted using a Dionex ASE 350 and a 9:1 mixture of dichloromethane:methanol. The total lipid extract was separated into apolar and polar fractions using alumina columns with 9:1 hexane:dichloromethane and 1:1 dichloromethane:methanol as eluents, respectively. The polar fraction was then filtered, and

branched glycerol dialkyl glycerol tetraethers were identified and quantified in 2016 (52). The apolar fraction was then dried and stored.

In 2025, the apolar fraction was further processed to isolate *n*-alkane leaf waxes. We first added a known quantity of 5 $\alpha$ -androstane to aid in quantifying leaf wax biomarkers. We then performed an additional, polarity-based separation using 5% deactivated silica gel columns to separate leaf wax *n*-alkanes (apolar alkyl lipids) from mildly polar compounds (e.g. ketone compounds). *n*-alkanes were eluted with hexane, and mildly polar compounds were eluted using dichloromethane. The isolated *n*-alkane leaf waxes were then quantified using a Thermo TRACE-1310 gas chromatograph with a programmable temperature vaporization inlet and a flame ionization detector. Once quantified, we measured the hydrogen and carbon isotopic composition of C<sub>31</sub> and C<sub>27</sub> leaf-waxes using a Delta V Plus isotope ratio mass spectrometer in continuous flow mode (Conflo IV) coupled to a Thermo TRACE-1310 through a GC-Isolink II. All samples were measured in duplicate to achieve a precision better than 2‰ for C<sub>31</sub>  $\delta D_{wax}$  and 0.2‰ for C<sub>31</sub>  $\delta^{13}C_{wax}$ . A synthetic *n*-alkane mix (A7 mix from Arndt Schimmelmann at Indiana University) was measured at regular intervals in between samples to monitor instrument drift and correct for any apparent offsets.

We assessed the fidelity of our  $\delta D_{wax}$  measurements at White Pond, SC to record  $\delta D_p$  with a core-top sample. For this core-top sample, we also measured  $\delta^{13}C_{wax}$  to correct for biosynthetic fractionation. We applied a two-end-member Bayesian mixing model to correct for leaf wax biosynthesis fractionation processes (53), yielding an estimate of  $\delta D_p$ . For C<sub>31</sub> alkanes, the reconstructed  $\delta D_p$  median estimate is -34.57‰ (95% CI: -40.12, -28.28) while the Online Isotopes in Precipitation Calculator (OIPC) (54) estimates an annual value of -28.43‰ ( $p = 0.058$ , Figure S5). In contrast, C<sub>27</sub> the  $\delta D_p$  reconstruction has a median estimate of -37.36‰ (95% CI: -42.73, -31.31). We perform all analyses on C<sub>31</sub> leaf waxes because the core-top  $\delta D_p$  estimate more closely matches OIPC (Figure S5).

$\delta D_{wax}$  measurements from Hall's Cave, TX were downloaded from the original publication (Supplementary Data 1 in (25)) in February 2026. Only C<sub>27</sub>  $\delta D_{wax}$  measurements are available for Hall's Cave; therefore, we replicate our analyses using C<sub>27</sub>  $\delta D_{wax}$  measurements from White Pond and find high agreement (Figure S6) suggesting our conclusions are insensitive to this analytical choice.

#### 4.2 $\Delta\delta D$ NASH<sub>leaf wax</sub> Calculation

We reconstructed variability in the North Atlantic Subtropical High across the last deglaciation using  $\delta D_{wax}$  measurements from White Pond, SC and Hall's Cave, TX and propagated temporal and measurement uncertainties using a Monte Carlo approach. We first generated new Bayesian age models for both sites using *Bacon* (55) and the chronological controls reported in each

publication (25, 52). For White Pond, we used the parameters in the original publication (52). These parameters were not recorded for Hall's Cave, so we use the default recommendations from *Bacon*. All *Bacon* parameters and corresponding code are freely available for review (48). We then defined a common temporal grid for interpolating  $\delta D_{\text{wax}}$ , spanning the overlapping age range of both records with a time step equal to the median temporal resolution across both sites.

To generate an ensemble of interpolated  $\delta D_{\text{wax}}$  records, we first propagated measurement uncertainty by randomly resampling  $\delta D_{\text{wax}}$  from  $N \left( \mu_{\text{wax}}, \frac{\sigma_{\text{wax}}}{\sqrt{N}} \right)$ , where  $N = 2$ , reflecting duplicate measurements at both sites. At White Pond,  $\mu_{\text{wax}}$  and  $\sigma_{\text{wax}}$  were estimated from the duplicate measurements directly. Individual  $\sigma_{\text{wax}}$  values were not reported for Hall's Cave, so we assigned  $\sigma_{\text{wax}} = 5$  based on measurement uncertainties described in the original publication and assume that reported  $\delta D_{\text{wax}}$  values estimate  $\mu_{\text{wax}}$  (25). Each resampled  $\delta D_{\text{wax}}$  record was then interpolated to the common temporal grid using age estimates drawn randomly from the posterior ensemble of the *Bacon* age models. Repeating this process 1,000 times produced an ensemble of interpolated  $\delta D_{\text{wax}}$  records that incorporate both age and measurement uncertainties. We standardized each ensemble member and subtracted the Hall's Cave ensemble from the White Pond ensemble, yielding 1,000 estimates of  $\Delta \delta D_{\text{NASH}_{\text{leaf wax}}}$ , from which we report the median and 95% confidence interval.

### 4.3 Climate simulations and contemporary climate data products

We examine the transient, deglacial isotope-enabled iTRACE experiments (43) to identify the dynamics of hydroclimate variability in ENA. The iTRACE experiments attempt to simulate climate evolution during the last deglaciation with the isotope-enabled Community Earth System Model v1.2 (iCESM). These simulations include transient changes in greenhouse gas concentrations, orbital configuration, ice sheets, and meltwater from 20,000 years before present (ka) to 11 ka. Simulations were performed at a nominal  $2^\circ$  horizontal resolution for the atmosphere and land model and  $1^\circ$  horizontal resolution for the ocean and sea ice models, with 30 vertical layers in the atmosphere.

The transient iTRACE experiments are compared against the iCESM simulations from Water Isotope Model Intercomparison Project (iCESM v1.3, WisoMIP) (40) experiments and the isotope-enabled Last Millennium Ensemble (iCESM v1, iLME) (40–42) to examine the sensitivity of the zonal  $\delta D_p$  gradient in southeastern North American to the North Atlantic Subtropical High. The WisoMIP simulations span 1979–2023 and are performed with only the atmosphere component of iCESM1.3 (i.e. iCAM5). Sea ice, sea surface temperatures, zonal and meridional winds, and atmospheric temperature were prescribed from ERA5 reanalysis throughout the simulation. This nudging corrects model biases and isolates the representation of

isotope systematics within iCESM1.3 (40). iLME spans the last 1,000 years (850 to 2006 CE) with transient solar intensity, volcanic emissions, greenhouse gases, aerosols, land use conditions, and orbital parameters as forcings (41, 42). Unlike WisoMIP, iLME is coupled to an ocean model and not nudged to correct for model biases. Both simulations were performed with a horizontal and vertical resolution comparable to iTRACE (41, 42). Together, this suite of simulations lets us assess whether mean-state biases or the response to forcings drive misrepresentation of the zonal  $\delta D_p$  gradient–North Atlantic Subtropical High relationship.

Within all models we calculate the integrated vapor transport as:

$$\mathbf{IVT} = \frac{1}{g} \int_{p_{top}}^{p_{sfc}} q \mathbf{V} dp$$

Where  $\mathbf{V}$  is horizontal winds,  $q$  is specific humidity,  $g$  is gravitational acceleration,  $p$  is pressure,  $p_s$  is surface pressure, and  $p_{top}$  is top of the atmosphere pressure.

#### 4.3.1 Reconciling the inverse $\delta D_p$ gradient–North Atlantic Subtropical High relationship in iTRACE

Unlike evidence from our proxy records, WisoMIP, and iLME, which demonstrate that an intensification and expansion of the North Atlantic Subtropical High increases the zonal  $\delta D_p / \delta D_{wax}$  gradient in southeastern North America (Figure 4), the simulated  $\delta D_p$  gradient in iTRACE (Figure 3) has an antiphase relationship to the North Atlantic Subtropical High. That is, an increase in the simulated zonal  $\delta D_p$  gradient in southeastern North America occurs when the North Atlantic Subtropical High has weakened and contracted (Figure 4C, S9). Composites comparing intervals of high ( $\geq 90$ th percentile) and low ( $\leq 10$ th percentile)  $\Delta \delta D$  NASH<sub>iCESM</sub> in iTRACE reinforce that the  $\delta D_p$  gradient in southeastern North America is still tied to a large-scale atmospheric reorganization centered on the North Atlantic (Figure 4C, S9). However, periods with a high zonal  $\delta D_p$  gradient in southeastern North America represent time intervals with a northward shift in the Intertropical Convergence Zone (e.g. Bølling-Allerød and Holocene) in response to a resumption of the Atlantic Meridional Overturning Circulation and a subsequent increase in North Atlantic temperature (Figure S7, S8). As the Intertropical Convergence Zone shifts northward following anomalously high temperatures in the North Atlantic (Figure S7, S8), positive precipitation anomalies in the subtropics decrease  $\delta D_p$  through the 'amount effect' (Figure S8)(56). A northward shift in the Intertropical Convergence Zone also produces easterly integrated vapor transport anomalies in the tropics. These anomalies transmit the negative  $\delta D_p$  signal to Hall's Cave, increasing the zonal  $\delta D_p$  gradient in southeastern North America (Figure 4D, S8). Since the Bølling-Allerød and Holocene represent increases in northern subtropical Atlantic temperatures (Figure S7), the North Atlantic Subtropical High weakens, likely from enhanced atmospheric column thickness over the northern subtropical

Atlantic relative to subpolar North Atlantic (Figure S8). Hence, the erroneous connection between the Intertropical Convergence Zone and Hall's Cave forces an increase in the zonal  $\delta D_p$  gradient in southeastern North America despite a weakening and contraction of the North Atlantic Subtropical High (Figure S9, S10).

#### **4.4 North Atlantic Subtropical High definition and metrics**

Within iTRACE, we examine variability in the North Atlantic Subtropical High using a modified version of the Bermuda High Index (BHI) from (29). The BHI is defined as the area weighted difference in mean sea level pressure between the Gulf of Mexico (25.38 - 29.38 °N, 95 - 90 °W) and the southern Great Plains (35 - 39 °N, 105.5 - 100 °W) and is designed, in part, to capture westward expansions in the North Atlantic Subtropical High (29). For instance, an intensification and westward expansion of the North Atlantic Subtropical High increases both the pressure gradient and the BHI, driving stronger northward winds into southeastern North America. To account for climate model mean-state biases in north Atlantic sea surface temperatures and corresponding mean sea level pressure across our different iCESM experiments and ERA5, we shift the Gulf of Mexico region five degrees east. That is, we define the Gulf of Mexico mean sea level pressures as the area weighted average between 25.38 - 29.38 °N, 85 - 80 °W (Figure 1). In addition, we standardize mean sea level pressure before taking the difference between the Gulf of Mexico and Great Plains to put both locations on a common scale, allowing both to equally contribute to the BHI.

## Figures

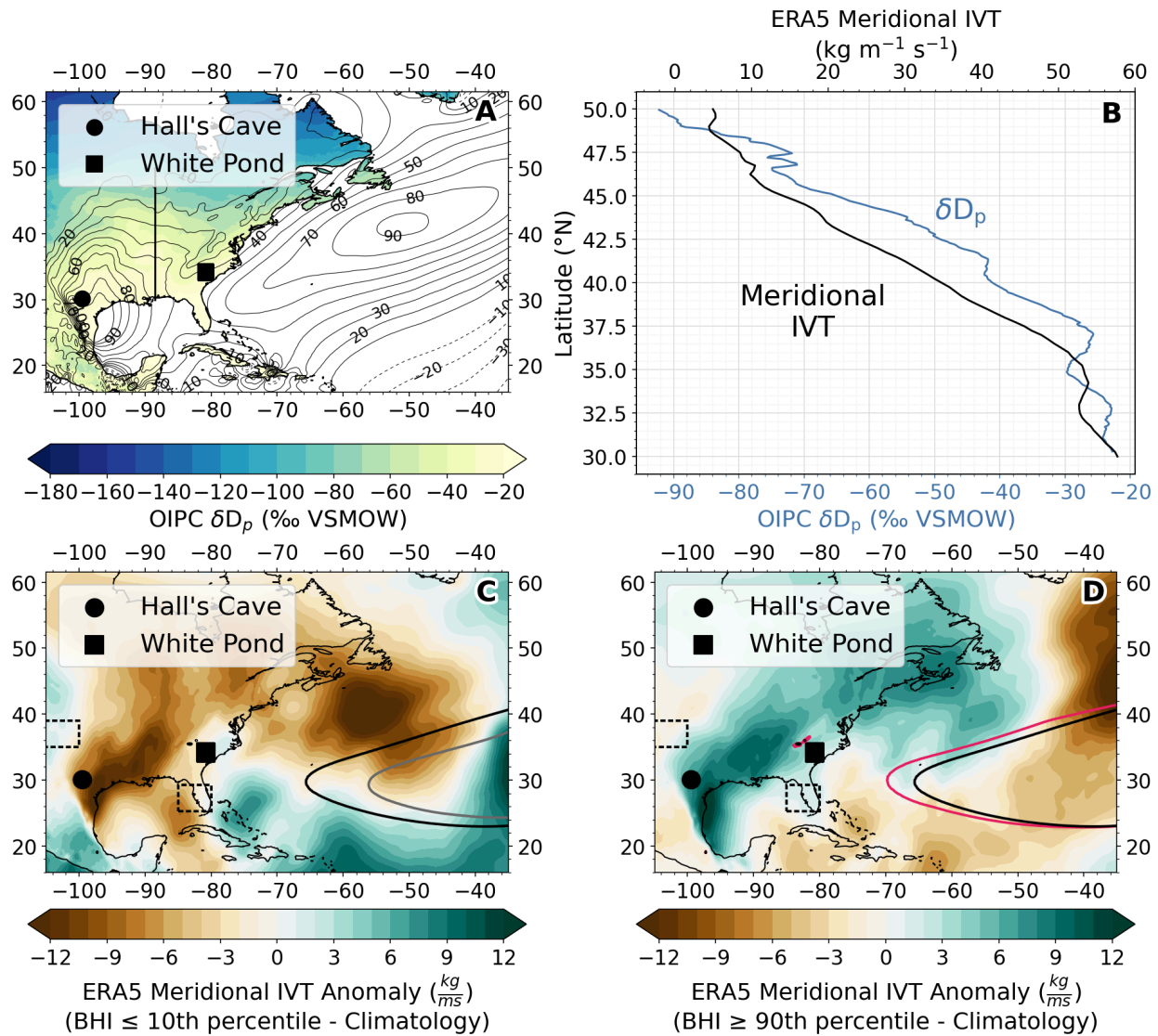


**Figure 1. The relationship between meridional moisture transport,  $\delta D_p$ , and the North Atlantic Subtropical High in southeastern North America, and the contrasting signals recorded by Hall's Cave and White Pond during shifts in North Atlantic Subtropical High spatial extent.** (A) The contemporary climatology of  $\delta D_p$  in SENA, where the filled contours correspond to  $\delta D_p$  and the black contours correspond to meridional integrated vapor transport from ERA5 with the 0 contour omitted. The black vertical line shows the transect presented in B. (B) A latitudinal transect at  $88.5^\circ \text{W}$  of integrated vapor transport (black line) and  $\delta D_p$  (blue line) between  $30^\circ$  and  $50^\circ \text{N}$ .  $\delta D_p$  values are from the Online Isotopes in Precipitation Calculator (54). (C) Map of meridional integrated vapor transport anomalies (filled contours) for an eastward contraction (BHI  $\leq 10$ th percentile) of the North Atlantic Subtropical High relative to the 1940 to 2024 average. The black contour corresponds to the climatological position of the 1019 hPa isobar, while the gray contour corresponds to the 1019 hPa isobar under an eastward contraction of the North Atlantic Subtropical High. D) As in C but for a westward expansion with the pink

contour corresponding to the 1019 hPa isobar under an westward expansion of the North Atlantic Subtropical High ( $BHI \geq 90$ th percentile) of the North Atlantic Subtropical High. Black dashed boxes in (C) and (D) correspond to the regions used to calculate BHI. In all mapped panels, the circle indicates Hall's Cave and the square indicates White Pond; these sites record contrasting signals during shifts in North Atlantic Subtropical High intensity and spatial extent.

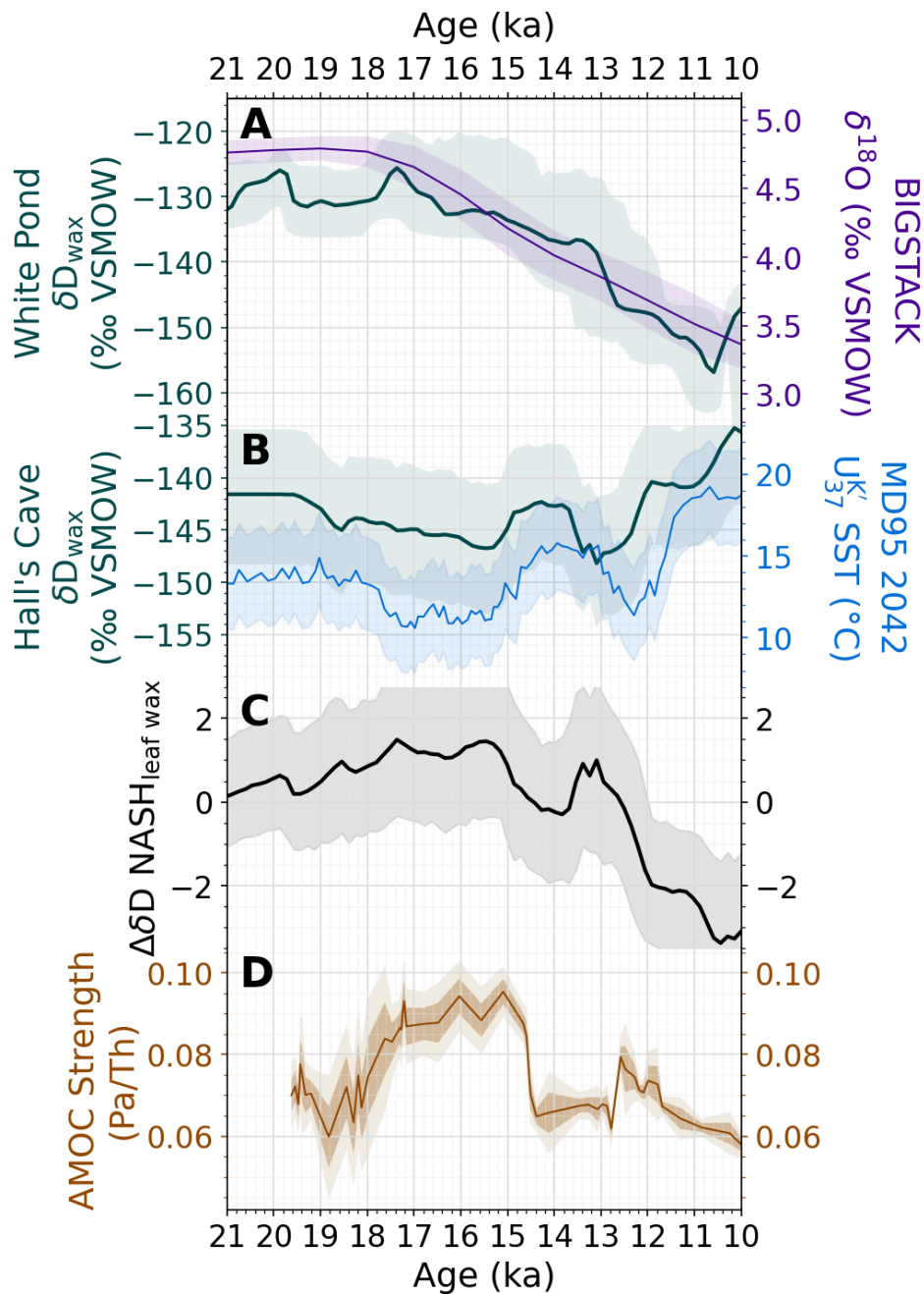


**Figure 2. North Atlantic Subtropical High evolution during the last deglaciation.** (A) Median White Pond  $\delta D_{wax}$  (green line, green shading represents the 95% CI) from a resampling approach that propagates measurement and temporal uncertainty compared benthic foraminifera  $\delta^{18}O$ , a proxy for global ice volume (purple line, purple shading represents 1- $\sigma$  measurement and temporal uncertainty) (57). (B) As in (A), but for Hall's Cave  $\delta D_{wax}$ , plus reconstructed north Atlantic sea surface temperatures from MD95 2042 (58) (shading representing the 95%

CI). (C) Median  $\Delta\delta D_{NASH_{leaf_{wax}}}$  values calculated as the standardized difference in  $\delta D_{wax}$  between White Pond and Hall's Cave (black line, gray shading represents the 95% CI), with temporal and measurement uncertainty propagated. (D) Reconstructed AMOC variability based on Pa/Th ratios in sediment cores from Bermuda Rise (13), with larger values representing a weaker AMOC (dark and light shading represent the 1- $\sigma$  and 2- $\sigma$  measurement uncertainty, respectively). A map of all site is present in the Supplemental Information (Figure S11).

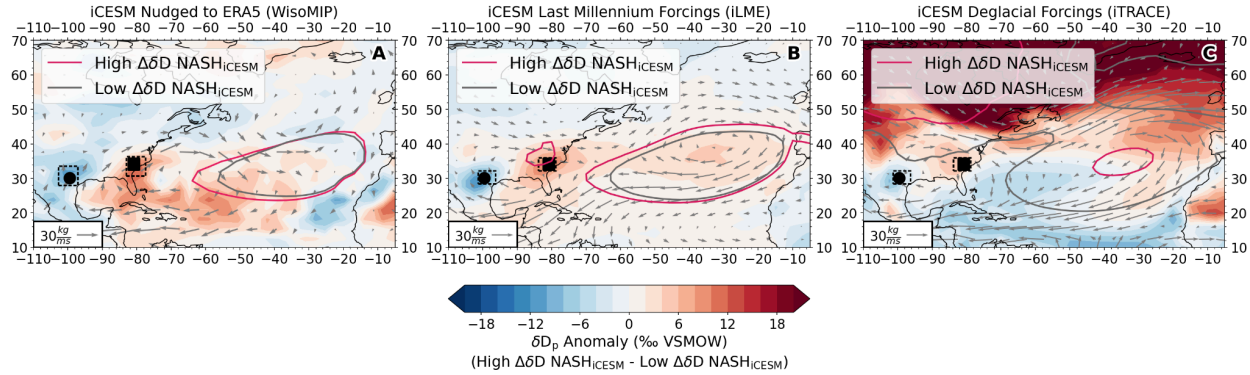


**Figure 3. Isotopic fingerprint of the North Atlantic Subtropical High.** Composites of mean sea level pressure (contours), integrated vapor transport (vectors), and  $\delta D_p$  (filled contours) from three iCESM experiments for high ( $\geq 90$ th percentile) - low ( $\leq 10$ th percentile)  $\Delta\delta D$  NASH<sub>iCESM</sub> years (40–43).  $\Delta\delta D$  NASH<sub>iCESM</sub> is defined identically to  $\Delta\delta D$  NASH<sub>leaf wax</sub>: the standardized difference between the four grid cells bounding White Pond and Hall's Cave simulated  $\delta D_p$ . For each experiment, the integrated vapor transport vectors and  $\delta D_p$  filled contours show the anomaly between high- $\Delta\delta D$  NASH<sub>iCESM</sub> and low- $\Delta\delta D$  NASH<sub>iCESM</sub> years. In contrast, the pink contour shows mean sea level pressure during high- $\Delta\delta D$  NASH<sub>iCESM</sub> years, while the gray contour shows mean sea level pressure during low- $\Delta\delta D$  NASH<sub>iCESM</sub> years, so the two contours together reveal how the simulated North Atlantic Subtropical High shifts in spatial extent and intensity. Note, given the different underlying boundary conditions we present the 1020 hPa contour in (A) and (B), but the 1030 hPa contour in (C).

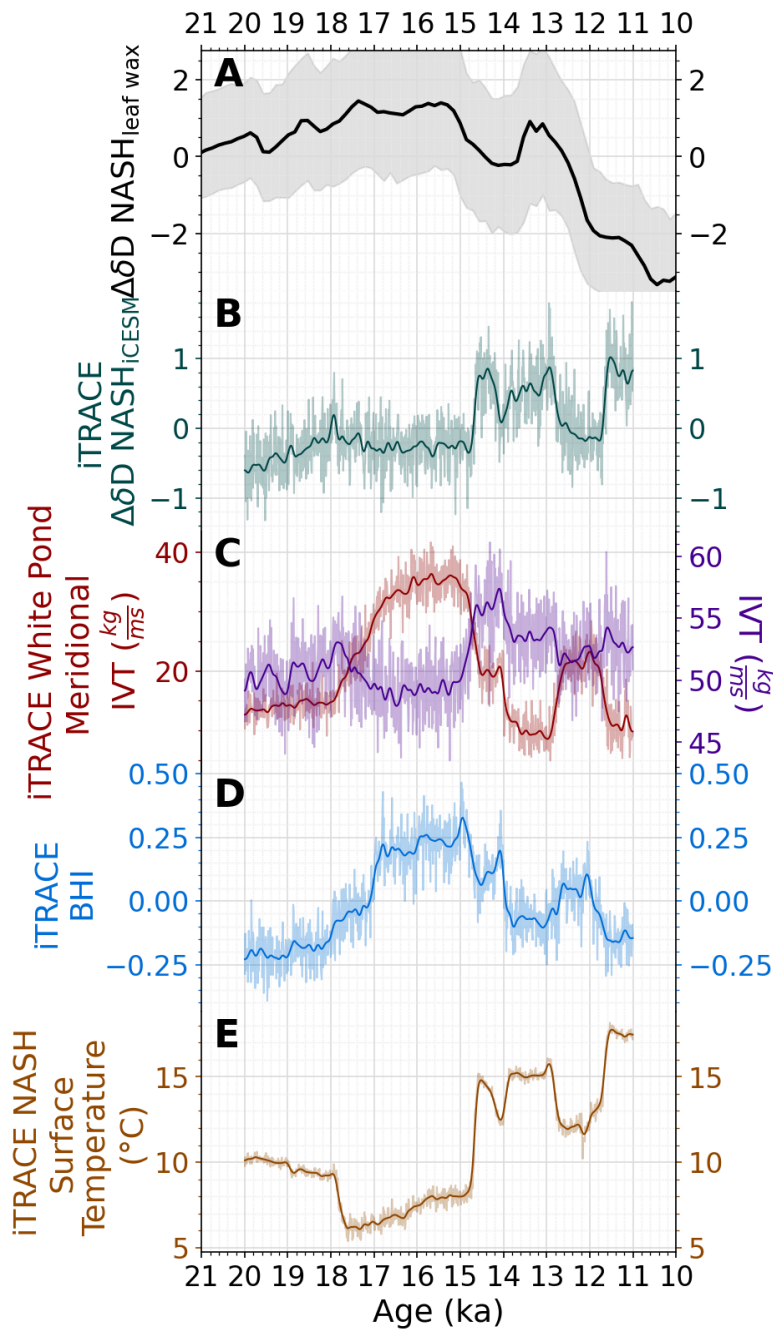


**Figure 4. iTRACE deglacial hydroclimate dynamics.** (A) Median  $\Delta\delta D$   $NASH_{leaf\ wax}$  values calculated as the standardized difference in  $\delta D_{wax}$  between White Pond and Hall's Cave (black line, gray shading represents the 95% CI), with temporal and measurement uncertainty propagated. (B)  $\Delta\delta D$   $NASH_{ICESM}$  calculated identically to (A) but from simulated  $\delta D_p$  for the four grid cells bounding White Pond and Hall's Cave from iTRACE. (C) Simulated meridional integrated vapor transport at White Pond (red line) and Hall's Cave (purple line). (D) Simulated iTRACE BHI, as used in Figure 1C and 1D. (E) Simulated North Atlantic iTRACE sea surface temperature, averaged between  $35^\circ$  to  $40^\circ N$  and  $55^\circ$  to  $65^\circ W$ . In panels B to E the light lines correspond to decadal averages and the dark lines correspond to a

Gaussian low-pass filter ( $\sigma = 50$  years).

## References

1. D. R. Easterling, K. E. Kunkel, J. R. Arnold, T. Knutson, A. N. LeGrande, L. R. Leung, “Precipitation change in the United States” in *Climate Science Special Report: A Sustained Assessment Activity of the U.S. Global Change Research Program*, D. J. Wuebbles, D. W. Fahey, K. A. Hibbard, D. J. Dokken, B. C. Stewart, T. K. Maycock, Eds. (U.S. Global Change Research Program, Washington, D.C., USA, 2017)vol. I, pp. 207–230.
2. J. Zhao, T. Y. Gan, G. Zhang, S. Zhang, Projected changes of precipitation extremes in North America using CMIP6 multi-climate model ensembles. *J. Hydrol.* **621**, 129598 (2023).
3. F. V. Davenport, M. Burke, N. S. Diffenbaugh, Contribution of historical precipitation change to US flood damages. *Proc. Natl. Acad. Sci.* **118**, e2017524118 (2021).
4. G. S. Benton, M. A. Estoque, Water-vapor transfer over the North American continent. *J. Atmospheric Sci.* **11**, 462–477 (1954).
5. E. M. Rasmusson, Atmospheric water vapor transport and the water balance of North America: Part I. Characteristics of the water vapor flux field. *Mon. Weather Rev.* **95**, 403–426 (1967).
6. H. M. Hasanean, Variability of the North Atlantic subtropical high and associations with tropical sea-surface temperature. *Int. J. Climatol.* **24**, 945–957 (2004).
7. M. J. Rodwell, B. J. Hoskins, Subtropical Anticyclones and Summer Monsoons. *J. Clim.* **14**, 3192–3211 (2001).
8. R. Grotjahn, *Global Atmospheric Circulations: Observations and Theories* (Oxford university press, New York Oxford, 1993).
9. W. Qiu, M. Collins, A. A. Scaife, Winter Subtropical Highs, the Hadley Circulation and Baroclinic Instability. *J. Geophys. Res. Atmospheres* **128**, e2023JD039604 (2023).
10. S. A. Marcott, T. K. Bauska, C. Buizert, E. J. Steig, J. L. Rosen, K. M. Cuffey, T. J. Fudge, J. P. Severinghaus, J. Ahn, M. L. Kalk, J. R. McConnell, T. Sowers, K. C. Taylor, J. W. C. White, E. J. Brook, Centennial-scale changes in the global carbon cycle during the last deglaciation. *Nature* **514**, 616 (2014).
11. P. U. Clark, J. D. Shakun, P. A. Baker, P. J. Bartlein, S. Brewer, E. J. Brook, A. E. Carlson, H. Cheng, D. S. Kaufman, Z. Liu, T. M. Marchitto, A. C. Mix, C. Morrill, B. L. Otto-Bliesner, K. Pahnke, J. M. Russell, C. Whitlock, J. F. Adkins, J. L. Blois, J. Clark, S. M. Colman, W. B. Curry, B. P. Flower, F. He, T. C. Johnson, J. Lynch-Stieglitz, V. Markgraf, J. F. McManus, J. X. Mitrovica, P. I. Moreno, J. W. Williams, Global climate evolution during the last deglaciation, *Proceedings of the National Academy of Sciences.* **109** (2012)pp. E1134–E1142.
12. A. S. Dalton, M. Margold, C. R. Stokes, L. Tarasov, A. S. Dyke, R. S. Adams, S. Allard, H. E. Arends, N. Atkinson, J. W. Attig, P. J. Barnett, R. L. Barnett, M. Batterson, P.

- Bernatchez, H. W. Borns, A. Breckenridge, J. P. Briner, E. Brouard, J. E. Campbell, A. E. Carlson, J. J. Clague, B. B. Curry, R.-A. Daigneault, H. Dubé-Loubert, D. J. Easterbrook, D. A. Franzi, H. G. Friedrich, S. Funder, M. S. Gauthier, A. S. Gowan, K. L. Harris, B. Hétu, T. S. Hooyer, C. E. Jennings, M. D. Johnson, A. E. Kehew, S. E. Kelley, D. Kerr, E. L. King, K. K. Kjeldsen, A. R. Knaeble, P. Lajeunesse, T. R. Lakeman, M. Lamothe, P. Larson, M. Lavoie, H. M. Loope, T. V. Lowell, B. A. Lusardi, L. Manz, I. McMartin, F. C. Nixon, S. Occhietti, M. A. Parkhill, D. J. W. Piper, A. G. Pronk, P. J. H. Richard, J. C. Ridge, M. Ross, M. Roy, A. Seaman, J. Shaw, R. R. Stea, J. T. Teller, W. B. Thompson, L. H. Thorleifson, D. J. Utting, J. J. Veillette, B. C. Ward, T. K. Weddle, H. E. Wright, An updated radiocarbon-based ice margin chronology for the last deglaciation of the North American Ice Sheet Complex, *Quaternary Science Reviews*. **234** (2020)p. 106223.
13. J. F. McManus, R. Francois, J. M. Gherardi, L. D. Keigwin, S. Brown-Leger, Collapse and rapid resumption of Atlantic meridional circulation linked to deglacial climate changes. *Nature* **428**, 834–837 (2004).
  14. D. Fastovich, J. M. Russell, S. A. Marcott, J. W. Williams, Spatial fingerprints and mechanisms of precipitation and temperature changes during the Younger Dryas in eastern North America. *Quat. Sci. Rev.* **294**, 107724 (2022).
  15. J. S. Salonen, F. Schenk, J. W. Williams, B. Shuman, A. L. Lindroth Dauner, S. Wagner, J. Jungclaus, Q. Zhang, M. Luoto, Patterns and drivers of Holocene moisture variability in mid-latitude eastern North America. *Nat. Commun.* **16**, 3582 (2025).
  16. B. N. Shuman, J. Marsicek, W. W. Oswald, D. R. Foster, Predictable hydrological and ecological responses to Holocene North Atlantic variability. *Proc. Natl. Acad. Sci.* **116**, 5985–5990 (2019).
  17. M. Chevalier, B. A. S. Davis, O. Heiri, H. Seppa, B. M. Chase, K. Gajewski, T. Lacourse, R. J. Telford, W. Finsinger, J. Guiot, N. Kuhl, S. Y. Maezumi, J. R. Tipton, V. A. Carter, T. Brussel, L. N. Phelps, A. Dawson, M. Zanon, F. Valle, C. Nolan, A. Mauri, A. de Vernal, K. Izumi, L. Holmstrom, J. Marsicek, S. Goring, P. S. Sommer, M. Chaput, D. Kupriyanov, Pollen-based climate reconstruction techniques for late Quaternary studies. *Earth-Sci. Rev.* **210**, 33 (2020).
  18. J. S. Salonen, M. Korpela, J. W. Williams, M. Luoto, Machine-learning based reconstructions of primary and secondary climate variables from North American and European fossil pollen data. *Sci Rep* **9**, 13 (2019).
  19. S. Juggins, Quantitative reconstructions in palaeolimnology: new paradigm or sick science? *Quat. Sci. Rev.* **64**, 20–32 (2013).
  20. D. Sachse, I. Billault, G. J. Bowen, Y. Chikaraishi, T. E. Dawson, S. J. Feakins, K. H. Freeman, C. R. Magill, F. A. McInerney, M. T. J. van der Meer, P. Polissar, R. J. Robins, J. P. Sachs, H. L. Schmidt, A. L. Sessions, J. W. C. White, J. B. West, A. Kahmen, “Molecular Paleohydrology: Interpreting the Hydrogen- Isotopic Composition of Lipid Biomarkers from Photosynthesizing Organisms” in *Annual Review of Earth and Planetary Sciences, Vol*

40, R. Jeanloz, Ed. (Annual Reviews, Palo Alto, 2012)vol. 40 of *Annual Review of Earth and Planetary Sciences*, pp. 221–249.

21. T. Bhattacharya, J. E. Tierney, P. DiNezio, Glacial reduction of the North American Monsoon via surface cooling and atmospheric ventilation. *Geophys. Res. Lett.* **44**, 5113–5122 (2017).
22. D. Fastovich, T. Bhattacharya, L. C. Pérez-Ángel, N. J. Burls, R. Feng, S. Knapp, T. Mayer, Large-scale sea surface temperature gradients govern westerly moisture transport in western Ecuador during the Plio-Pleistocene. *Earth Planet. Sci. Lett.* **640**, 118781 (2024).
23. S. J. Feakins, Pollen-corrected leaf wax D/H reconstructions of northeast African hydrological changes during the late Miocene. *Palaeogeogr. Palaeoclimatol. Palaeoecol.* **374**, 62–71 (2013).
24. J. E. Tierney, J. M. Russell, Y. S. Huang, J. S. S. Damste, E. C. Hopmans, A. S. Cohen, Northern hemisphere controls on tropical southeast African climate during the past 60,000 years. *Science* **322**, 252–255 (2008).
25. C. Sun, T. M. Shanahan, P. N. DiNezio, N. P. McKay, P. D. Roy, Great Plains storm intensity since the last glacial controlled by spring surface warming. *Nat. Geosci.* **14**, 912–917 (2021).
26. N. L. Ingraham, B. E. Taylor, Light stable isotope systematics of large-scale hydrologic regimes in California and Nevada. *Water Resour. Res.* **27**, 77–90 (1991).
27. J. M. Welker, Isotopic ( $\delta^{18}\text{O}$ ) characteristics of weekly precipitation collected across the USA: an initial analysis with application to water source studies. *Hydrol. Process.* **14**, 1449–1464 (2000).
28. K. Rozanski, L. Araguás-Araguás, R. Gonfiantini, “Isotopic Patterns in Modern Global Precipitation” in *Climate Change in Continental Isotopic Records* (American Geophysical Union (AGU), 1993; <https://onlinelibrary.wiley.com/doi/abs/10.1029/GM078p0001>), pp. 1–36.
29. J. Zhu, X.-Z. Liang, Impacts of the Bermuda High on Regional Climate and Ozone over the United States. *J. Clim.* **26**, 1018–1032 (2013).
30. C. Sun, T. M. Shanahan, J. Partin, Controls on the Isotopic Composition of Precipitation in the South-Central United States. *J. Geophys. Res. Atmospheres* **124**, 8320–8335 (2019).
31. F. Song, Z. Feng, L. R. Leung, R. A. H. Jr, J. Wang, J. Hardin, C. R. Homeyer, Contrasting Spring and Summer Large-Scale Environments Associated with Mesoscale Convective Systems over the U.S. Great Plains. *J. Clim.* **32**, 6749–6767 (2019).
32. F. Song, L. R. Leung, J. Lu, L. Dong, Future Changes in Seasonality of the North Pacific and North Atlantic Subtropical Highs. *Geophys. Res. Lett.* **45**, 11,959–11,968 (2018).

33. W. Zhou, L. R. Leung, F. Song, J. Lu, Future Changes in the Great Plains Low-Level Jet Governed by Seasonally Dependent Pattern Changes in the North Atlantic Subtropical High. *Geophys. Res. Lett.* **48**, e2020GL090356 (2021).
34. A. Brauer, G. H. Haug, P. Dulski, D. M. Sigman, J. F. W. Negendank, An abrupt wind shift in western Europe at the onset of the Younger Dryas cold period. *Nat. Geosci.* **1**, 520–523 (2008).
35. F. S. R. Pausata, C. Li, J. J. Wettstein, M. Kageyama, K. H. Nisancioglu, The key role of topography in altering North Atlantic atmospheric circulation during the last glacial period. *Clim. Past* **7**, 1089–1101 (2011).
36. F. S. R. Pausata, C. Li, J. J. Wettstein, K. H. Nisancioglu, D. S. Battisti, Changes in atmospheric variability in a glacial climate and the impacts on proxy data: a model intercomparison. *Clim. Past* **5**, 489–502 (2009).
37. L. M. Baldini, F. McDermott, J. U. L. Baldini, P. Arias, M. Cueto, I. J. Fairchild, D. L. Hoffmann, D. P. Matthey, W. Muller, D. C. Nita, R. Ontanon, C. Garcia-Monco, D. A. Richards, Regional temperature, atmospheric circulation, and sea-ice variability within the Younger Dryas Event constrained using a speleothem from northern Iberia. *Earth Planet. Sci. Lett.* **419**, 101–110 (2015).
38. D. Fastovich, J. M. Russell, S. T. Jackson, T. R. Krause, S. A. Marcott, J. W. Williams, Spatial fingerprint of Younger Dryas cooling and warming in eastern North America. *Geophys. Res. Lett.* **47**, e2020GL090031 (2020).
39. N. El bani Altuna, M. M. Ezat, L. Smik, F. Muschitiello, S. T. Belt, J. Knies, T. L. Rasmussen, Sea ice-ocean coupling during Heinrich Stadials in the Atlantic–Arctic gateway. *Sci. Rep.* **14**, 1065 (2024).
40. H. Bong, A. N. LeGrande, S. Dee, J. Zhu, A. Cauquoin, R. P. Fiorella, Q. Ding, N. Dutrievoz, M. Tanoue, M. Frazer, M. Sarkar, C. Agosta, K. Yoshimura, M. Werner, A. Okazaki, C. Risi, H. C. Steen-Larsen, M. Casado, S. Wahl, J. Nusbaumer, J. Worden, S. Good, A. Bailey, M. Schneider, S. Noël, S. Mandal, K. Bowman, Y. Li, G. A. Schmidt, Water Isotope Model Intercomparison Project (WisOMIP): Present-Day Climate. *J. Geophys. Res. Atmospheres* **131**, e2025JD044985 (2026).
41. B. L. Otto-Bliesner, E. C. Brady, J. Fasullo, A. Jahn, L. Landrum, S. Stevenson, N. Rosenbloom, A. Mai, G. Strand, Climate Variability and Change since 850 CE: An Ensemble Approach with the Community Earth System Model. *Bull. Am. Meteorol. Soc.* **97**, 735–754 (2016).
42. S. Stevenson, B. L. Otto-Bliesner, E. C. Brady, J. Nusbaumer, C. Tabor, R. Tomas, D. C. Noone, Z. Liu, Volcanic Eruption Signatures in the Isotope-Enabled Last Millennium Ensemble. *Paleoceanogr. Paleoclimatology* **34**, 1534–1552 (2019).
43. C. He, “Deciphering the Deglacial Evolution of Water Isotope and Climate in the Northern Hemisphere,” thesis, The Ohio State University, United States -- Ohio (2021).

44. D. A. Bishop, A. P. Williams, R. Seager, Increased fall precipitation in the southeastern United States driven by higher-intensity, frontal precipitation. *Geophys. Res. Lett.* **46**, 8300–8309 (2019).
45. A. G. Pendergrass, D. L. Hartmann, Changes in the Distribution of Rain Frequency and Intensity in Response to Global Warming. *J. Clim.* **27**, 8372–8383 (2014).
46. N. Teale, D. A. Robinson, Long-term variability in atmospheric moisture transport and relationship with heavy precipitation in the eastern USA. *Clim. Change* **175**, 1 (2022).
47. W. Li, L. Li, M. Ting, Y. Liu, Intensification of Northern Hemisphere subtropical highs in a warming climate. *Nat. Geosci.* **5**, 830–834 (2012).
48. D. Fastovich, T. Bhattacharya, S. Jackson, T. Krause, J. Russell, T. Shanahan, C. Sun, J. Williams, Code and Data for Deglacial reconstruction of the spatial extent and intensity of the North Atlantic Subtropical High, version 1, Zenodo (2026); <https://doi.org/10.5281/ZENODO.20628395>.
49. E. B. B. Otto-Bliesner, R. Tomas, Z. Liu, C. He, iTraCE (2021). <https://doi.org/10.26024/b290-an76>.
50. B. Otto-Bliesner, E. Brady, J. Fasullo, A. Jahn, L. Landrum, S. Stevenson, N. Rosenbloom, A. Mai, W. Strand, CESM1 Last Millennium Ensemble, NSF National Center for Atmospheric Research (2025); <https://doi.org/10.5065/C32Y-RK84>.
51. T. R. Krause, J. M. Russell, R. Zhang, J. W. Williams, S. T. Jackson, Late-Quaternary vegetation, climate, and fire history of the Southeast Atlantic Coastal Plain based on a 30,000-yr multi-proxy record from White Pond, South Carolina (USA). *Quat. Res.* <https://doi.org/10.1017/qua.2018.95> (2019).
52. T. R. Krause, J. M. Russell, R. Zhang, J. W. Williams, S. T. Jackson, Late Quaternary vegetation, climate, and fire history of the Southeast Atlantic Coastal Plain based on a 30,000-yr multi-proxy record from White Pond, South Carolina, USA. *Quat. Res.*, 1–20 (2019).
53. J. E. Tierney, F. S. R. Pausata, P. B. deMenocal, Rainfall regimes of the Green Sahara. *Sci. Adv.* **3**, e1601503 (2017).
54. G. J. Bowen, Gridded maps of the isotopic composition of meteoric waters, (2025).
55. M. Blaauw, J. A. Christen, Flexible paleoclimate age-depth models using an autoregressive gamma process. *Bayesian Anal.* **6**, 457–474 (2011).
56. J. Hu, J. Emile-Geay, J. Nusbaumer, D. Noone, Impact of Convective Activity on Precipitation  $\delta^{18}\text{O}$  in Isotope-Enabled General Circulation Models. *J. Geophys. Res. Atmospheres* **123**, 13,595–13,610 (2018).

57. Y. Zhou, L. E. Lisiecki, S. R. Meyers, T. Lee, C. Lawrence, Global and regional Pleistocene benthic  $\delta^{18}\text{O}$  stacks with a comparison of different age modeling strategies. *Geochronology* **8**, 85–107 (2026).
58. N. Davtian, E. Bard, A new view on abrupt climate changes and the bipolar seesaw based on paleotemperatures from Iberian Margin sediments. *Proc. Natl. Acad. Sci.* **120**, e2209558120 (2023).

### Supplemental Figures

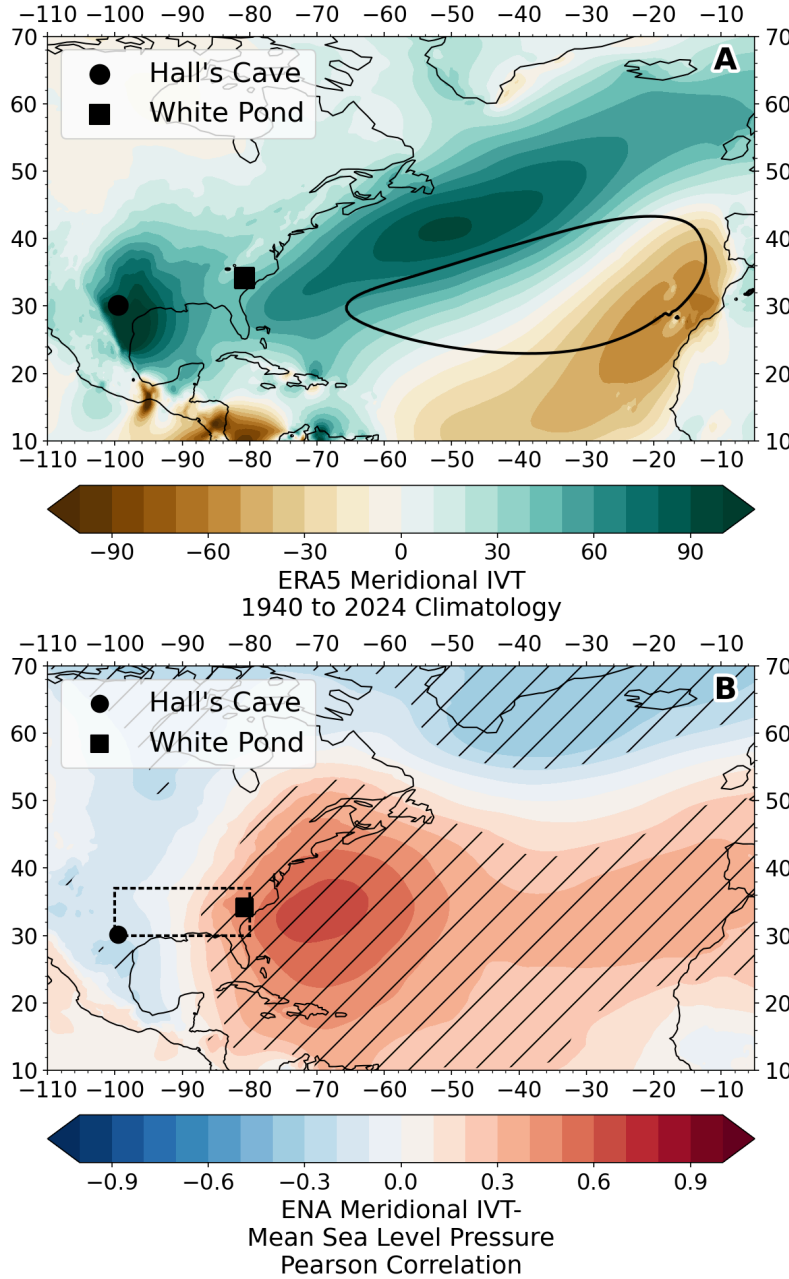


**Figure S1.** (A) The 1940 to 2024 climatology of meridional integrated vapor transport in southeastern North America and the 1019 hPa isobar (black contour) from ERA5. (B) The Pearson correlation between meridional integrated vapor transport into southeastern North America (black dashed box) and mean sea level pressure. Regions with significant correlations are denoted with hashing. Significant correlations over the Atlantic suggest that the geostrophic balance between the North Atlantic Subtropical High and low pressure over eastern North America drive meridional moisture flux into southeastern North America.

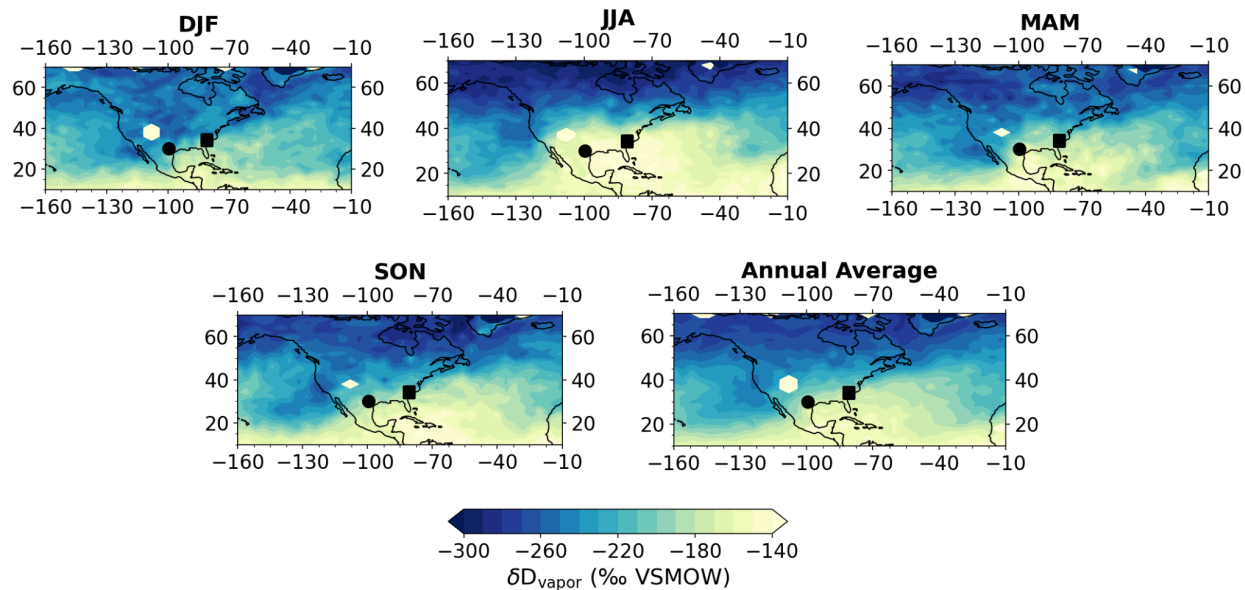


**Figure S2.** Seasonal and annual climatology of  $\delta D_{\text{vapor}}$  from the tropospheric emission spectrometer. Estimates are pressure-weighted and averaged between 825 and 450 hPa. The square and circle points correspond to White Pond and Hall's Cave, respectively. Post-processed data is from (22).

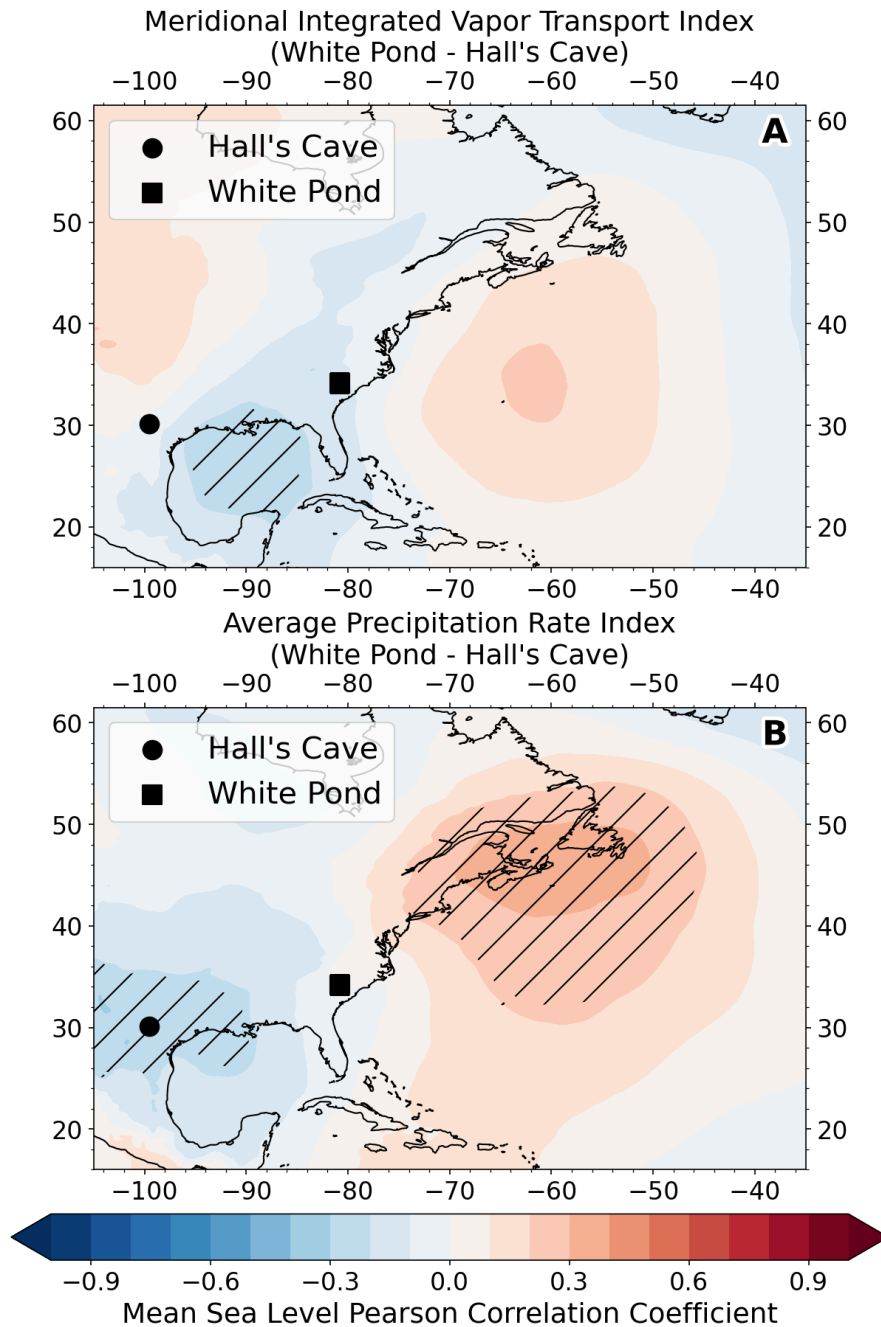


**Figure S3.** (A, B) The filled contours correspond to the Pearson correlation between indices that replicate  $\Delta\delta D$  NASH, but with meteorological fields from ERA5. (A) The standardized difference between meridional integrated vapor transport at White Pond and Hall's Cave is compared to mean sea level pressure. Regions with significant correlations are denoted with hashing. Significant correlations over the Gulf of Mexico suggest that westward expansions in the North Atlantic Subtropical High are correlated with the difference in meridional integrated vapor transport between our two sites. (B) The standardized difference between average precipitation rate at White Pond and Hall's

Cave is compared to mean sea level pressure. Regions with significant correlations are denoted with hashing. Significant correlations over the Atlantic suggest that the intensity of the North Atlantic Subtropical High is correlated with the difference in average precipitation rate between our two sites.

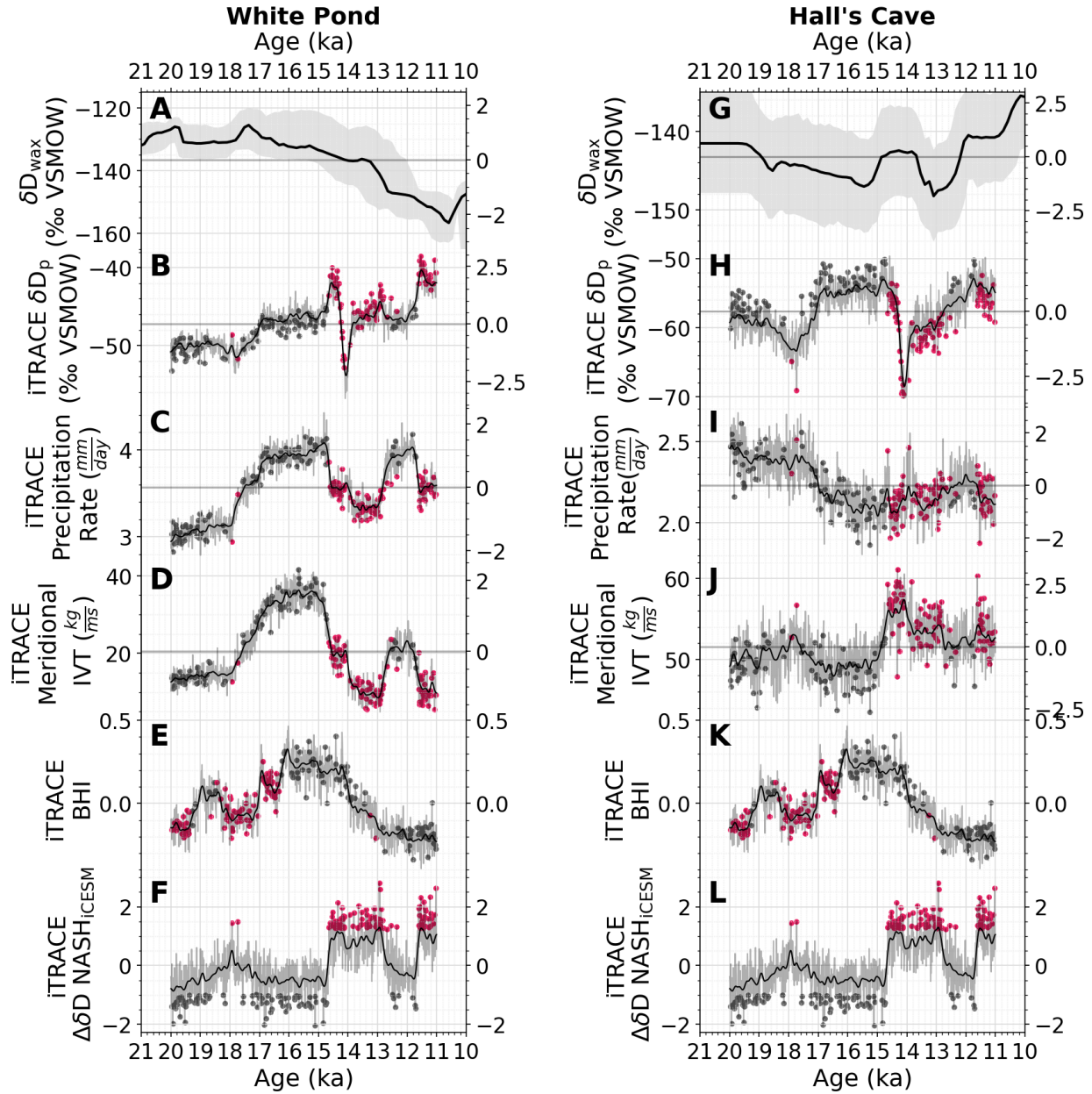


**Figure S4.** Measured  $\delta D_{\text{wax}}$  from (A) White Pond and (G) Hall's Cave with temporal and measurement uncertainty propagated through a resampling approach compared to simulated, iTRACE, time series of site-level (B, H)  $\delta D_p$ , (C, I) precipitation rate, and (D, J) meridional integrated vapor transport. (E, K) Simulated BHI from iTRACE. (F, L)  $\Delta\delta D \text{ NASH}_{\text{iCESM}}$  calculated identically to  $\Delta\delta D \text{ NASH}_{\text{leaf wax}}$ . In all iTRACE panels (B-F, H-L), the pink points correspond to time periods when  $\Delta\delta D \text{ NASH}_{\text{iCESM}} \geq 90\text{th percentile}$ . The gray points correspond to time periods when  $\Delta\delta D \text{ NASH}_{\text{iCESM}} \leq 10\text{th percentile}$ . Except for (A) and (G), the light gray line corresponds to decadal averages and the dark lines correspond to a Gaussian low-pass filter ( $\sigma = 50$  years). In A-D and G-J, the right y-axis corresponds to standardized values with the horizontal line representing standardized values of 0.

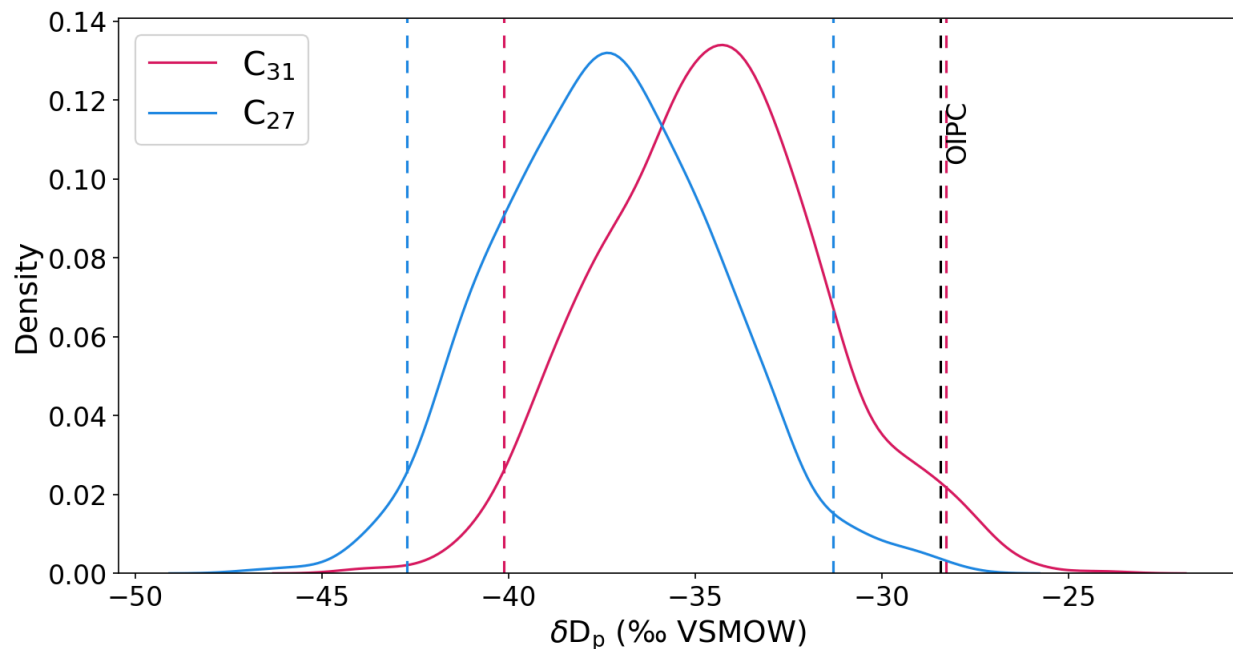


**Figure S5.** The posterior distribution of predicted  $\delta D_p$  for core top sediment from White Pond where predictions are from a two-end member Bayesian mixing model (53).  $\delta D_p$  was reconstructed for  $C_{31}$  and  $C_{27}$  leaf waxes, with  $C_{31}$  showing a closer agreement to observations from the Online Isotopes in Precipitation Calculator. The colored dashed lines correspond to the 95% confidence interval for reconstructed  $\delta D_p$ . The second dashed line near  $-28\text{‰}$  for  $C_{31}$  is near the black dashed line. The black dashed line corresponds to  $\delta D_p$  for the closet grid cell to White Pond from the Online Isotopes in Precipitation Calculator (54).

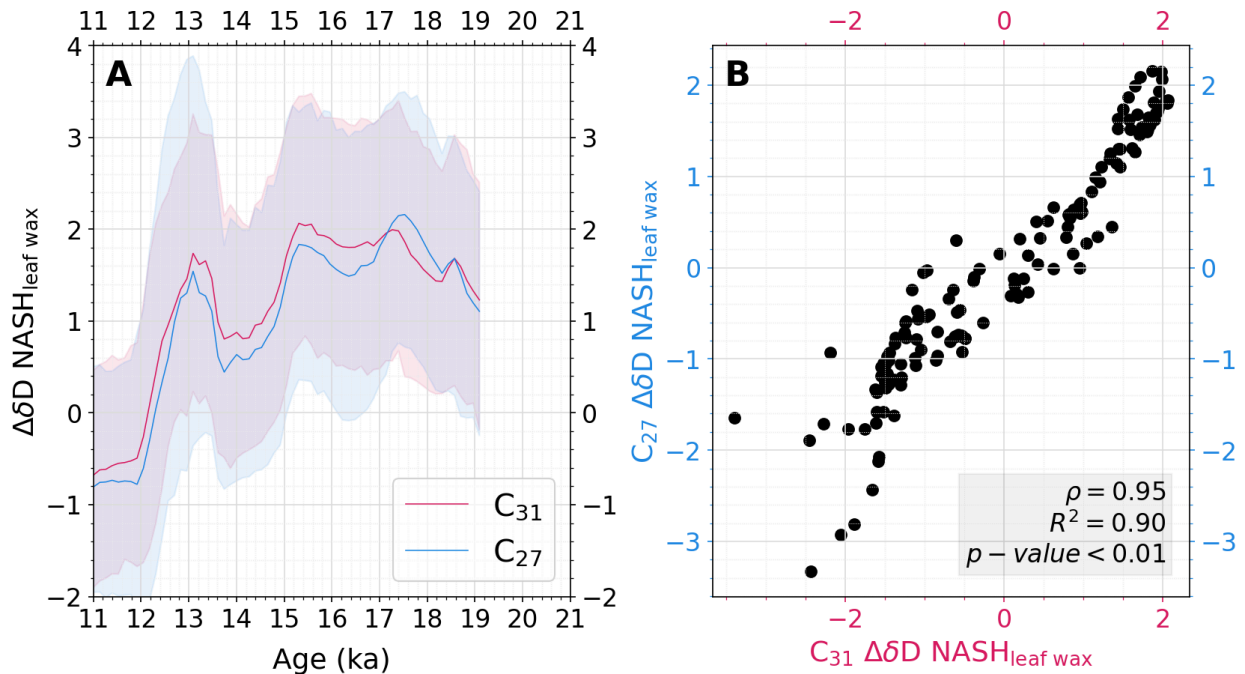


**Figure S6.** (A) A comparison of North Atlantic Subtropical High reconstructions using  $C_{31}$  (pink) and  $C_{27}$  (blue) chain length alkanes from White Pond and  $C_{27}$  alkanes from Hall's Cave. (B) A crossplot of paired North Atlantic Subtropical High reconstructions from (A). Note the high similarity between reconstructions and high correlation. This suggests that our North Atlantic Subtropical High reconstruction is not sensitive to our analytical decision to focus on  $C_{31}$  alkanes at White Pond.

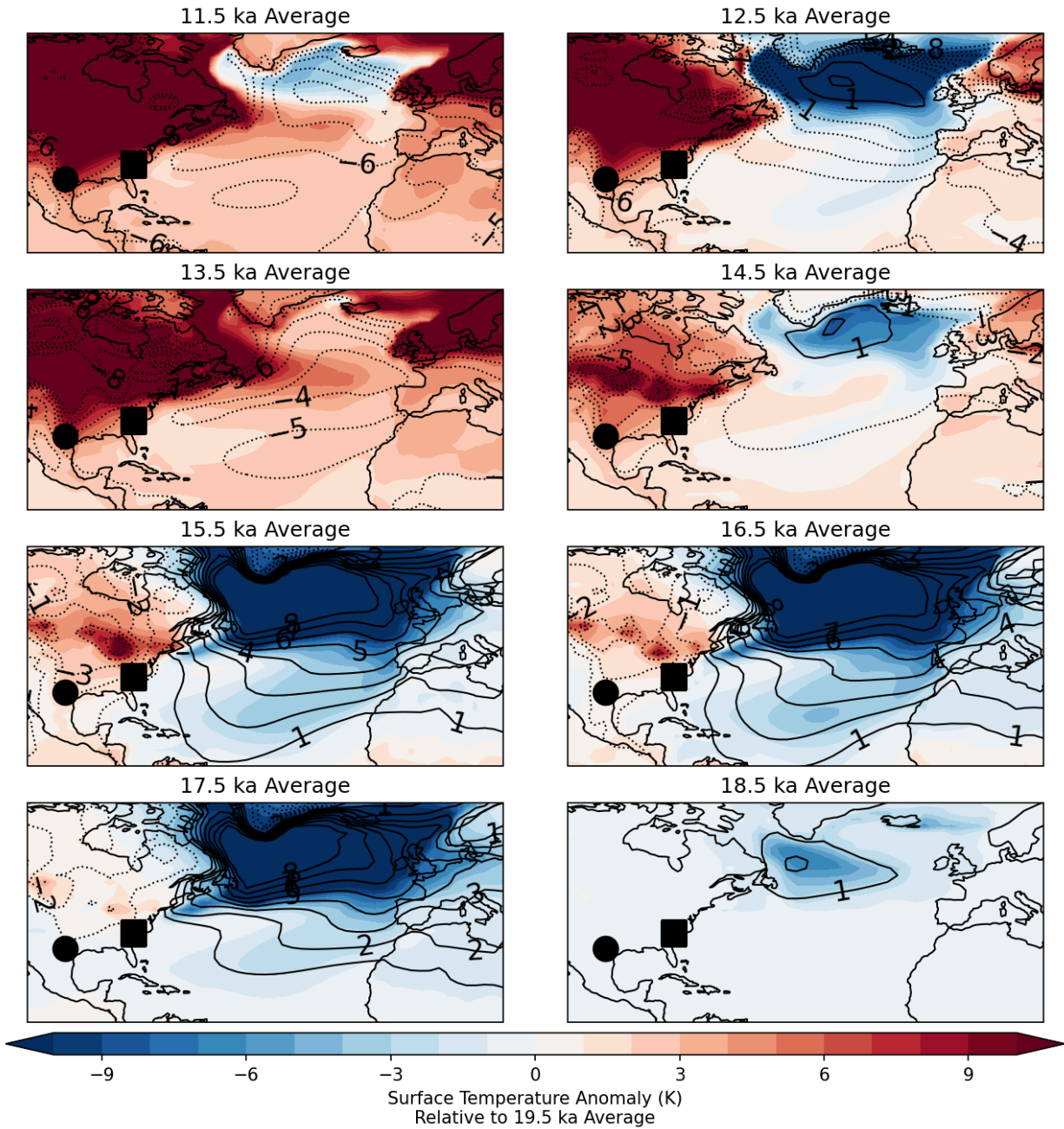


**Figure S7.** Millennial averages of surface temperature and mean sea level pressure relative to a Last Glacial Maximum baseline (20 to 19 ka). The square and circle points correspond to White Pond and Hall's Cave, respectively.

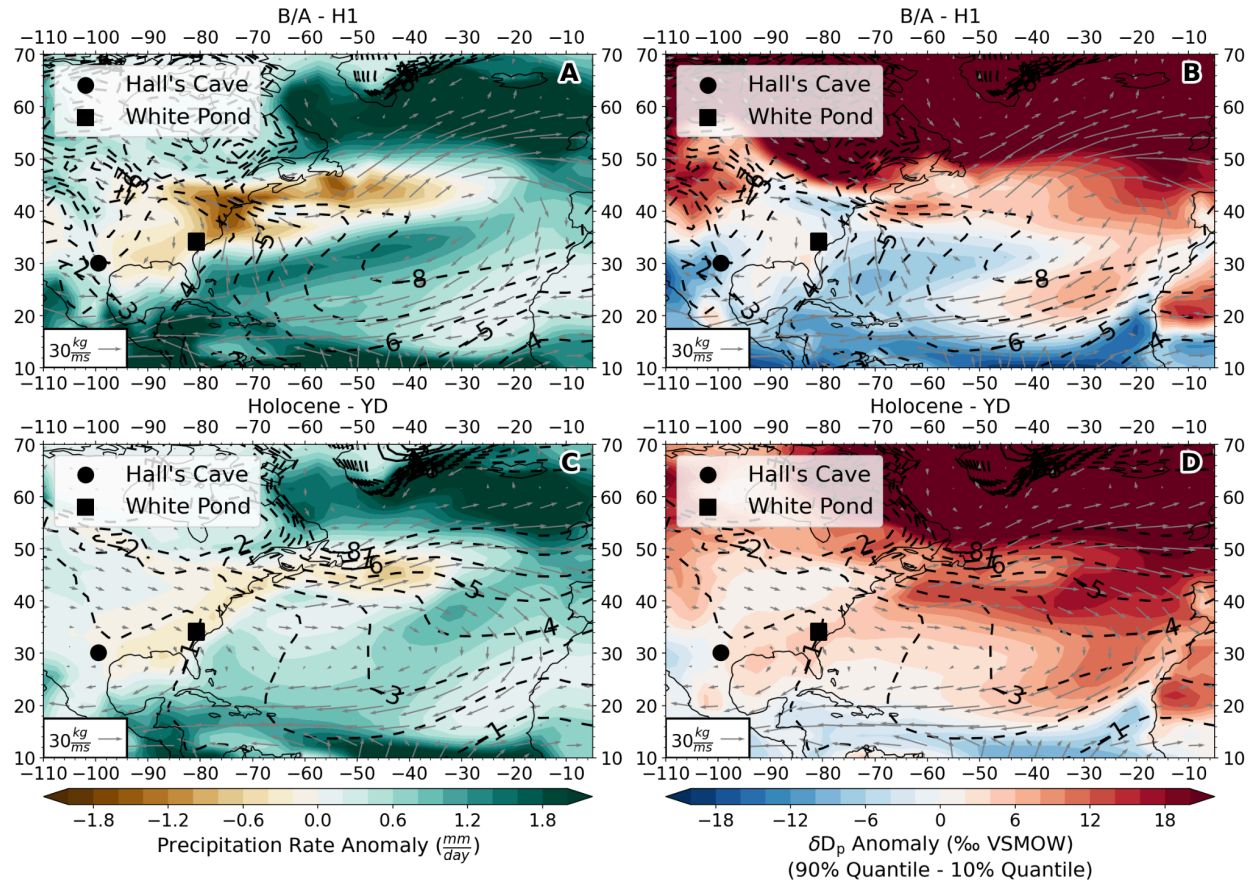


**Figure S8.** Anomaly fields of simulated (A, C) precipitation rate (filled contours), (B, D)  $\delta D_p$ , (A-D) integrated vapor transport, and (A-D) mean sea level pressure diagnosing the causes of the inverse southeastern North American  $\delta D_p$  gradient-North Atlantic Subtropical High relationship in iTRACE. (A, B) The Heinrich event 1 (temporal average from 17 ka to 15 ka) is subtracted from the Bølling-Allerød (temporal average from 14 ka to 13 ka). Large positive precipitation anomalies in the subtropical and tropical Atlantic from a northward shift in the Intertropical Convergence Zone correspond with decreases in  $\delta D_p$  from the ‘amount effect’. Low subtropical and tropical Atlantic  $\delta D_p$  is transmitted to Hall’s Cave through easterly anomalies in integrated vapor transport despite decreases in mean sea level pressure. (C, D) The Younger Dryas (temporal average from 12.9 ka to 11.7 ka) is subtracted from the Holocene (temporal average from 11.7 ka to 11 ka, when the iTRACE experiment ends). The spatial patterns in (C, D) mirror (A, B).

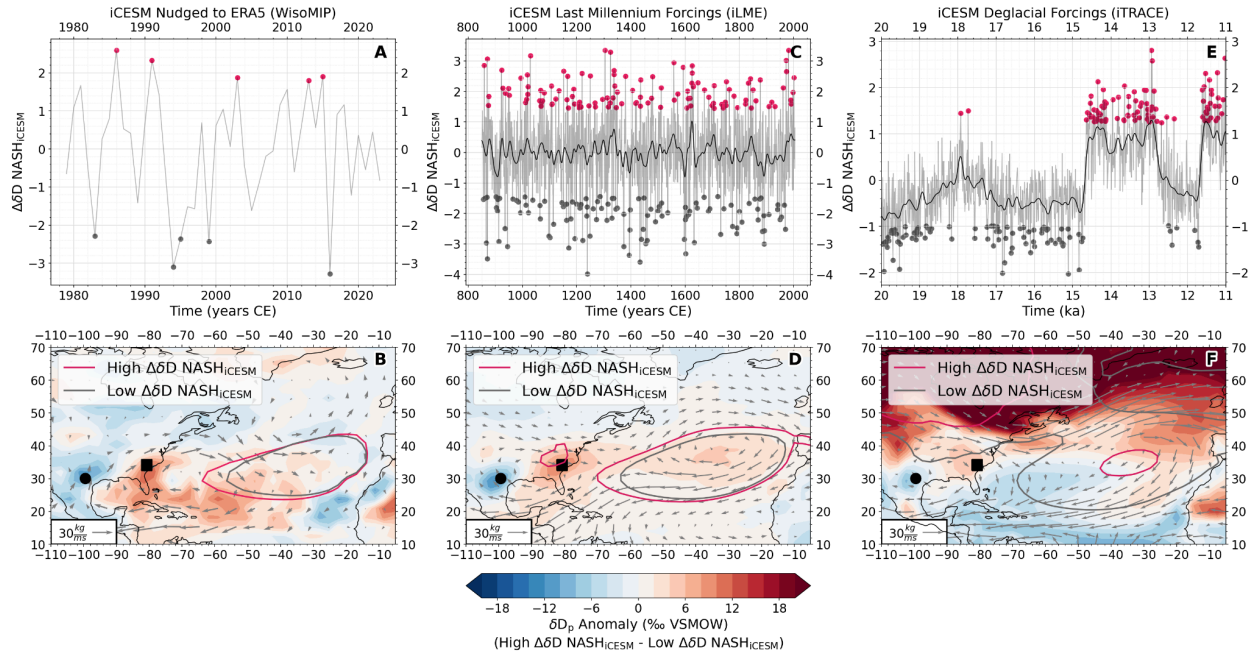


**Figure S9.** (B, D, F) As in Figure 4, but with the corresponding simulated North Atlantic  $\Delta\delta\text{D NASH}_{i\text{CESM}}$  time series (A, C, E). The pink points correspond to time periods when  $\Delta\delta\text{D NASH}_{i\text{CESM}} \geq 90\text{th percentile}$ . The gray points correspond to time periods when  $\Delta\delta\text{D NASH}_{i\text{CESM}}$ . The anomaly fields in B, D, and F represent the difference in the average of the pink and gray points from A, C, and E and are identical to Figure 3.

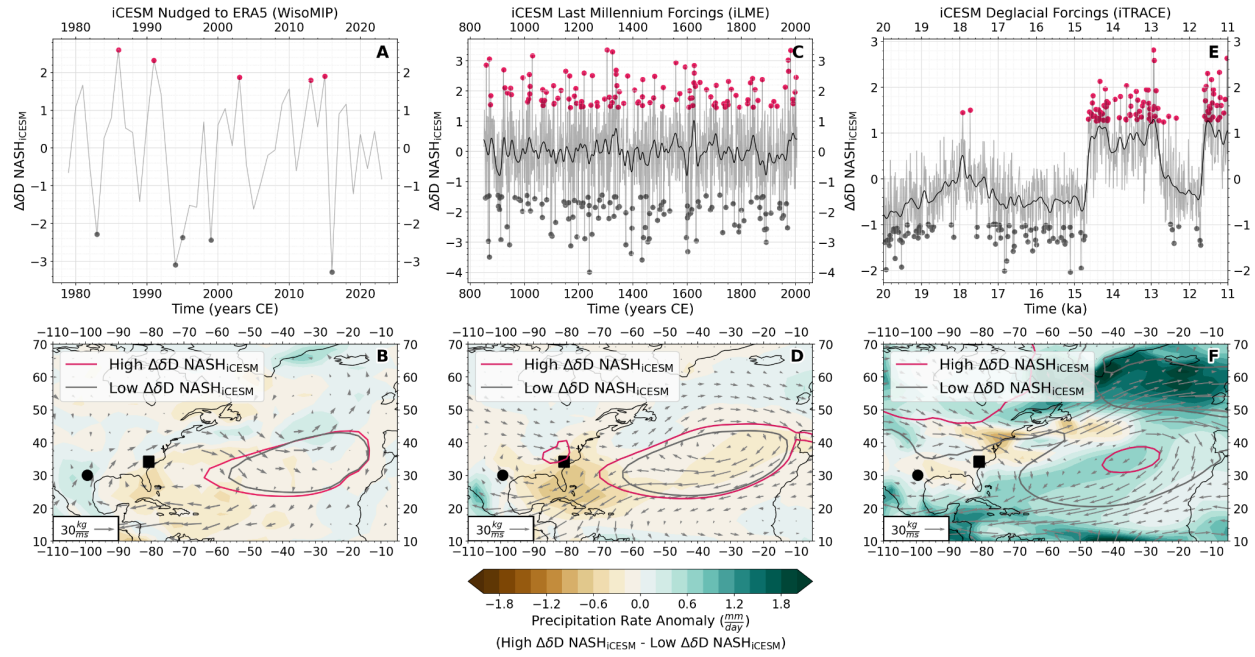


**Figure S10.** (B, D, F) As in Figure S9 but for simulated precipitation rate anomalies.

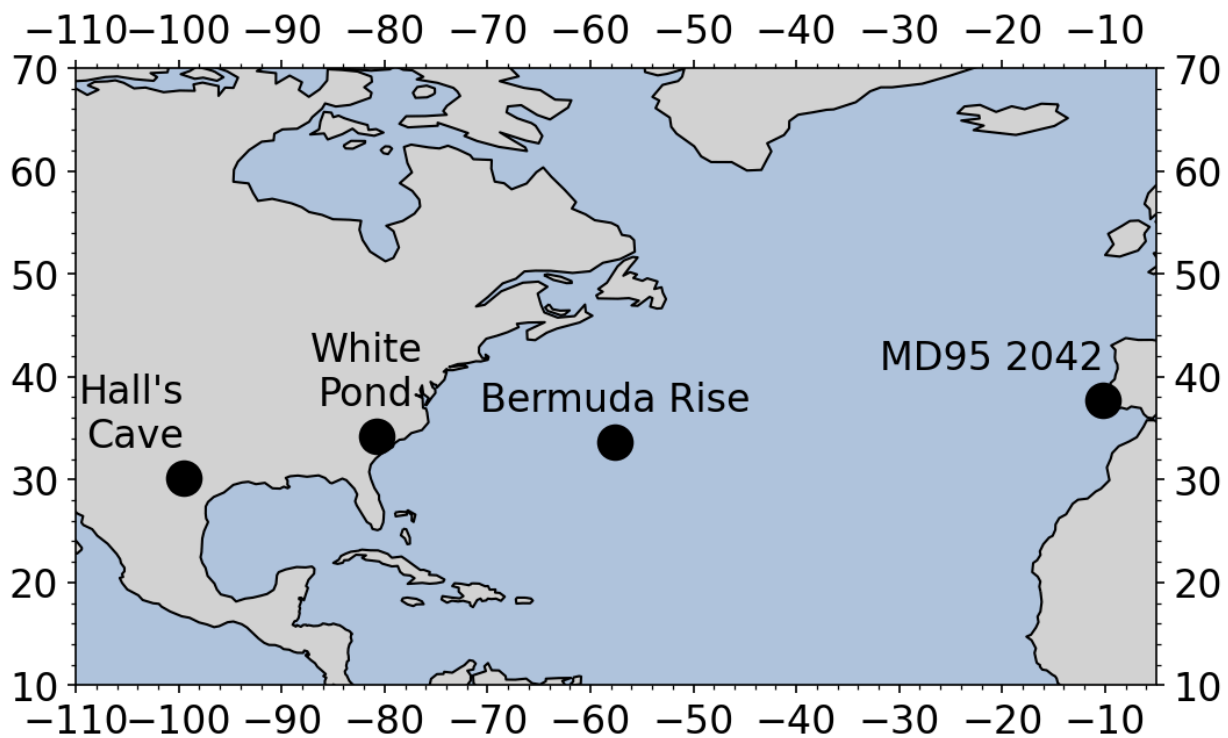


**Figure S11.** A map of all sites used for analyses in Figures 2 and 4.